Nanowires for Ultraviolet-Visible-Infrared Optoelectronic Synaptic Devices

*Xue Chen, Bingkun Chen, Bei Jiang, Tengfei Gao, Gang Shang, Su-Ting Han, Chi-Ching Kuo, Vellaisamy A. L. Roy and Ye Zhou**

X. Chen, G. Shang
Institute of Microscale Optoelectronics, Shenzhen University, Shenzhen 518060, P. R. China

B. Chen
College of Physics and Optoelectronic Engineering, Harbin Engineering University, Harbin 150001, P. R. China.

B. Jiang
Faculty of Physics and Electronic Science, Hubei University, Wuhan 430062, P. R. China.

T. Gao
Department of Electrical and Computer Engineering, University of California, Davis, California 95616, USA

Prof. S.-T. Han
College of Electronics and Information Engineering, Shenzhen University, Shenzhen 518060, P. R. China.

Prof. C.-C. Kuo
Institute of Organic and Polymeric Materials, Research and Development Center of Smart Textile Technology, National Taipei University of Technology, Taipei 10608, Taiwan.

Prof. V. A. L. Roy
James Watt School of Engineering, University of Glasgow, Glasgow, G12 8QQ UK.

Prof. Y. Zhou
Institute for Advanced Study, Shenzhen University, Shenzhen 518060, P. R. China
E-mail: yezhou@szu.edu.cn

Keywords: nanowires; optoelectronic synapse; ultraviolet-visible-infrared; synaptic functionalities; neuromorphic applications.

Abstract: Simulating biological synaptic functionalities through artificial synaptic devices opens up an innovative way to overcome the von Neumann bottleneck in device level. Artificial optoelectronic synapses provide a non-contact method to operate the devices and overcome the shortcomings of electrical synaptic devices. With the advantages of high photoelectric conversion efficiency, adjustable light absorption coefficient, and broad spectral range, nanowires based optoelectronic synapses have attracted wide attention. Herein, to better promote the applications of nanowires based optoelectronic synapses for future neuromorphic systems, the functionalities of optoelectronic synaptic devices and the current progress of nanowires optoelectronic synaptic devices in ultraviolet-visible-infrared spectral range are introduced. Furthermore, a bridge between nanowires based optoelectronic synaptic device and neuromorphic system is established. Challenges for the forthcoming development of nanowires optoelectronic synapses are also discussed. This review may offer a vision into the design and neuromorphic applications of nanowires based optoelectronic synaptic devices.

1. Introduction

Owing to the physical separation of memory module and processing module in von Neumann architecture-based computers, the traditional computers suffer from the problems of high power consumption and low computation speed, which limits their applications in Internet of Things and artificial intelligence.[1-4] The human brain is capable of storing and processing data at the same time, thus high-speed and low power consumption (only 1-100 fJ) can be attained easily in human brain.[5-7] Moreover, intelligent activities, i.g. pattern recognition, self-learning, problem processing, can also be completed by the human brain.[8-10] Thus, neuromorphic computing have attracted widespread attention and considered as an efficient way to break the von Neumann bottleneck. In human brains, the realization of intelligent functionalities is dependent on the neurons and synapses. A signal in the form of an action potential is transferred from one neuron to another through synapses.[11-13] Almost ~ 10^{11} neurons and ~ 10^{15} synapses exist in our brain,[5, 14] and the numerous neurons and synapses allow the human brain to perform complex neural activities. Thus, mimicking the biological functionalities of synapses are critical for neuromorphic applications.[15-16]

Since the idea of brain-like computing and the term of neuromorphic are proposed in 1948 and 1980s,[17] artificial electronic synaptic devices have been quickly developed. Lots of synaptic functionalities can be mimicked, such as short-term plasticity, long-term plasticity, spike-rating-dependent plasticity (SRDP), spike-timing-dependent plasticity (STDP), and so on.[18-20] These synaptic functionalities will be described in detail later. Artificial electronic synaptic devices have emerged as a very promising technological approach to be applied in artificial neural networks (ANNs) and artificial intelligence. Silicon based electronic synaptic devices have been fabricated as early as 1998,[21] subsequently, various artificial synaptic devices, i.g. memristors,[22] field-effect transistors (FETs),[23] phase change memory,[24] and ferroelectric memory,[25] have been successively developed to mimic synaptic behaviors. The fabrication of electronic integrated circuits is relatively simple. So far, the electronic circuits of electronic synaptic devices have been relatively mature. Although great progress has been made in artificial electronic synaptic devices, some challenges still remain to be faced: the purely electrical input/output limit the functional diversity of the devices;[26] the speed of neural operations is not ideal owing to the limit of bandwidth-connection-density trade-off;[27] the large RC delay and power loss associated with electrical integration.[28-29] Artificial photonic synaptic devices provide a noncontact method to operate the devices and can overcome the above shortcomings. Photonic synapses can be divided into two types: pure photonic synapses and optoelectronic synapses. Owing to the unique advantages of wide bandwidth, high interference immunity, low RC delay and power loss, photonic synapse is more suitable for high speed computing system.[30] Pure photonic synapses show the advantages of ultrahigh speed, large bandwidth, and no electrical interconnect power loss.[31] The synaptic weight in pure photonic synapse is determined by the optical transmission in the device, thus the operation speed of the device may be limited by the transformation process in the optical-structures. And the fabrication process of pure photonic synapse is very complex. For optoelectronic synapse, the synaptic weight is determined by the conductivity of the device. Although both optical and electrical singles are needed to operate the optoelectronic synapses, the optoelectronic synapses are more similar to biological synapses. The comparison of key characteristics for electronic, optoelectronic, and pure photonic synapses is performed in **Table 1**. Besides, optoelectronic synaptic devices have the ability to integrate visual signal sensing, information processing, and data memory, which is important for neuromorphic computing owing to the fact that most information is obtained through biological visual cortex system in human beings.[32] Consequently, extensive efforts have been dedicated to the development of optoelectronic synapses.[33-34]

Recent years, with the fast development of semiconductor technology, nanomaterial-based artificial optoelectronic synaptic devices, including zero-dimensional (0D) materials,[35-36] one-dimensional (1D) materials,[37-39] and two-dimensional (2D) materials,[40-41] have gotten wildly attention.[42]. Among these nanomaterials, quasi-1D geometry nanowires (NWs), with the characteristics of antenna-like shape, high aspect ratio, large surface-to-volume ratio, high carrier mobility and sub-wavelength size effect, usually show high photoelectric conversion efficiency and adjustable light absorption coefficient.[43-45] The NWs absorption cross-section may be far greater than the NWs cross-sectional area.[46] The low dimensionality leads to shorter photo-generated carrier transport time. The large surface-to-volume ratio leads to rich surface states, resulting in prolonged photo-generated carrier lifetime. Thus, substantial photoconductive gains are achieved in NWs optoelectronic devices.[47] Furthermore, NWs can cover wide-ranging spectrum from ultraviolet to infrared. Based on the band energy, GaN and oxide NWs (i.e. ZnO, Ga_2O_3, SnO_2, MoO_x) show significant photo absorption to ultraviolet light;[33, 48-50] Perovskite, CdS, and CdSe are suitable for detecting visible light;[51-53] Besides, traditional Si and III-V semiconductors have been confirmed to be applied in infrared.[51, 54-57] Actually, the spectral range of the materials is not limited by the band edge. Photoresponse can be produced as long as the photon energy is larger than the bandgap of the materials. Different spectral ranges correspond to different application prospects. These issues will be discussed in the part III. More importantly, NWs can possess positive and negative photoconductivity simultaneously,[58-59] which can achieve all-optical-controlled synaptic behaviors in one device. Thus, NWs exhibit potential application prospects in optoelectronic artificial synapses.

Here, we focus on the optoelectronic synaptic devices based on NWs for ultraviolet-visible-infrared applications. First, we introduce the basic functionalities of artificial optoelectronic synapses and summarize the NWs materials located in different wavelength. Then the potential applications of NWs optoelectronic synaptic devices at different wavelength are discussed. Finally, we propose an outlook of semiconductor NWs enabled optoelectronic artificial synapses for future multifunctional neuromorphic systems. The overview of this review article is illustrated in **Figure 1**.[60-64]

2. NWs Growth and Optoelectronic Synaptic Characteristics

2.1 Growth of NWs

At nanoscale, only a small change can result in a large impact on the performance of the NWs based device. Therefore, controlling the size and shape of NWs are critical. The challenges of

growing NWs include effectively controlling the size, orientation, structure, phase purity, and chemical composition. The behavior of charge carriers in electronic devices is affected by the size of NWs. The application of NWs based device requires uniform NWs diameters. The crystalline phase of NWs, whether zinc blende or wurtzite, will directly affect the energy band structures and electronic properties. In addition, crystal defects, such as stacking faults and twinnings, can produce non-radiative recombination centers, which will influence the performance of optoelectronic devices. Controlling chemical composition to realize intrinsic or doped NWs and NWs based heterojunctions are also essential technologies. NWs can be grown by a variety of methods, which can be divided into two categories: top-down approach and bottom-up approach. The top-down approach is originated from bulk materials. NWs are patterned by combining both lithography and etching, such as using electron beam lithography, plasma etching, and focused ion beam milling. The top-down approach has been fixed in the microelectronics industry. However, according to Moore's law, the channel length of the device needs to continue to shrink. The top-down approach presents more and more problems. Owing to the limit in resolution of lithography and etching techniques, difficulty arises in defining parameters for smaller dimensions and the quality of the NWs decreases. The etching and patterning processes also introduce surface defects that strongly affect the NWs properties. In addition, these processes are inherently wasteful, and many difficulties still need to be overcome before these technologies become high-output and low-cost methods for the growth of NWs.

On the other hand, the bottom-up approach involves the chemical synthesis of NWs, so their properties can be effectively controlled and regulated during the growth process. These NWs are themselves building blocks that can be assembled into more complex nanoscale devices and systems. The bottom-up approach is different from the top-down approach. The bottom-up approach offers opportunities to fabricate atomically precise and complex devices, which is benefit for the application of next generation nanoscale electronic and optoelectronic devices. The bottom-up approach mimics the growth of organisms in many ways, so it can assemble into larger and more complex structures. In the bottom-up growth method, there are mainly two NWs growth techniques: template-guided approach and free-standing approach.

Template-guided approach can limit the crystal growth to 1D NWs shape by template, that is, only 1D growth is allowed, and growth in other directions is physically restricted. The template may be porous anodized aluminum, diblock copolymer, V-shaped groove and step edges. These templates allow reasonable control over the diameter and length of NWs, and can be easily integrated with existing devices. However, the success of these techniques is

entirely dependent on the ability to fabricate suitable templates, and the quality of the templates directly affects the quality of the grown NWs. In the case of growth using templates, the template material limits the types of NWs materials that can be grown. Meanwhile, the NWs still remain on the substrate, which makes it impossible to assemble into complex device structures. Finally, the control of the size of NWs is limited by the resolution of the patterned template technique.

The free-standing NWs growth method relies on the anisotropy of the growth rate. Typically, NWs nucleate at a single point and extend along the growth direction with the highest growth rate, while other directions grow at a slower rate, constraining NWs to 1D. Many growth mechanisms have been used to grow free-standing NWs, including self-catalytic growth, oxide-assisted growth, vapor-liquid-solid (VLS) growth, and solution-liquid-solid growth. NWs can be grown in solution or liquid phase, and can also be suspended in a growth medium or in contact with a substrate to achieve growth. The VLS growth is the most widely used method, which is originated from 1964. It is proposed by Wagner and Ellis to explain the anisotropy of Au-catalyzed Si NWs.[65] VLS growth process contains vapor, liquid, and solid.[66] The Si precursor is introduced in the gas phase, and the Au particles and Si form a liquid eutectic alloy at the growth temperature. With the further feeding of Si, the Au-Si alloy particles become supersaturated, and Si precipitates at the Au-semiconductor interface, forming solid Si NWs. Two mechanisms can be used to explain the growth of NWs. First, due to the high holding coefficient of the liquid phase, the liquid particles are favorable collection points for reactive species in the gas phase, thus facilitating the growth of NWs; second, the metal particles are chemical catalysts, which lower the activation energy barrier and enhance the gas phase decomposition of precursors.[67] The techniques that are widely chosen for NWs growth include chemical vapor deposition (CVD),[46] metal-oganic chemical vapor deposition (MOCVD),[68] and molecular beam epitaxy (MBE).[68-69] MBE has an ultra-high vacuum environment, which is easy to grow higher-purity NWs. At the same time, MBE can achieve precise tuning in growth process of NWs. In addition, the reflection high-energy electron diffraction attached to the MBE system can strictly control the growth process,[70] especially in the growth process of NWs based heterojunctions and related structures.

2.2 Working Mechanisms of NWs Optoelectronic Synapses

To design NWs optoelectronic synapses which are more suitable for neuromorphic application, it is necessary to understand the working mechanisms of NWs optoelectronic

synapses. Here, we briefly describe two classical working mechanisms of NWs optoelectronic synapses, including trap states and band engineering.

2.2.1 Trap States

Carrier transport processes in semiconductor optoelectronic devices can be regulated by the trap states in semiconductors, including surface defect states, interface defect states, and bulk defects.[71-73] Owing to the large surface-to-volume ratio of NWs, surface state is a key factor affecting the carrier transport processes of NWs optoelectronic devices.[50] When photo-generated carriers are generated by light, some photo-generated carriers are recombined in a relatively short time, while some photo-generated carriers are separated by electric field and collected by electrodes, resulting in postsynaptic current (PSC). Due to the rich surface states of NWs, lots of the photo-generated carriers will be trapped by the surface states before recombination and collection, resulting in prolonged carrier lifetime. Synaptic weights can be changed by modulating the trapped/detrapped processes of photo-generated carriers.

2.2.2 Band Engineering

The design of band alignment is an efficient way to modulate the trapped processes of photo-generated carriers. By the design of heterojunction, PN junction, and Schottky junction, barriers and built-in electrical fields will be produced at the interfaces, which can suppress or promote the separation and recombination of photo-generated carriers.[74-76] Besides, some complex structures are also used to modulate the transport processes of photo-generated carriers, such as quantum well,[77] superlattice,[37] and 2D electron-hole tube structure.[78] Through rational band engineering, the trapping and recombination of photo-generated carriers in NWs can be controlled, thus the optoelectronic synaptic weights are modulated.

2.3. Basic Functionalities of Synaptic Devices

For artificial synapses, they can mimic the basic functionalities of biological synapses. The schematic diagram of artificial and biological synapse structures is shown in **Figure 2**a. In biological synapses, the synaptic functionalities are realized by the connection strength between pre-synaptic and post-synaptic neurons, i.e. synaptic weight.[53] The modification of synaptic weight is defined as synaptic plasticity, which plays a key role in the transmission of information in human brains.[79] In artificial synaptic devices, synaptic plasticity is usually described as the changes of specific physical parameters, such as resistivity and conductivity. For human brain, synaptic plasticity is the basis of memory and learning processes. Hebbian learn rule was proposed in 1949, which can describe the synaptic plasticity well.[42] Current measurements are often performed to analyze the synaptic functionalities upon external

stimulation. The PSC will be changed when an external stimulation is applied at presynaptic membrane. When the PSC becomes larger after stimulation, it means excitation, and the current is named as excitation postsynaptic current (EPSC), which is shown in Figure 2b; as the PSC becomes smaller after stimulation, it means inhibition, and the current is inhibition postsynaptic current (IPSC), which can be seen in Figure 2c.[80] For EPSC, after removing the stimulation, the channel current will gradually decay to a relative low value over time. The decay current can be fitted by the Kohlrausch stretched exponential function, which is similar as the Ebbinghaus forgetting curve in human brain:[81-83]

$$I = I_{\infty} + \left(I_0 - I_{\infty}\right)\exp\left[-\left(\frac{t-t_0}{\tau}\right)^{\beta}\right] \quad (1)$$

where I is the instantaneous current, I_0 is the EPSC triggered by presynaptic spikes, I_∞ is the stabilized state decay current, τ is the decay constant, which means the retention time of the device, t_0 is the finished time of presynaptic spikes, and β is the stretch index (between 0 and 1). The value of τ is related to the memory function of the device. When τ is large, the device shows excellent memory property.[84] To better promote the development of artificial synapses, it is essential to understand synaptic plasticity. In this part, we will introduce the synaptic plasticity, and discuss the basic functionalities of synaptic devices, including short-term and long-term plasticity, as well as transition from short-term plasticity to long-term plasticity.

2.3.1. Short-term Plasticity

Short-term plasticity includes short-term potentiation/depression (STP/STD), which is related to the recognition and processing of human brain upon external signals. Short-term plasticity depends on the neural response properties, therefore the recognized information will be forgotten easily.[85] Paired pulse facilitation (PPF), paired pulse depression (PPD) and spike-number-dependent plasticity (SNDP) are typical forms of short-term plasticity, as shown in Figure 2e-g.When the synaptic device is stimulated by two consecutive pulses, it responds more or less to the second stimulus than to the first, resulting in PPF or PPD.[86] A simulation of PPF and PPD are shown in Figure 2e and 2f. The PPF/PPD index can be extracted by[34, 87]

$$\text{PPF index} = \left[\left(A_2 - A_1\right)/A_1\right] \times 100\% \quad (2)$$

$$\text{PPD index} = \left[\left(B_1 - B_2\right)/B_1\right] \times 100\% \quad (3)$$

where A_1/B_1 is the first stimulus current, and A_2/B_2 is the second one. The PPF and PPD index will vary with the time interval between two successive stimuli (Δt). The relationship between PPF (PPD) index and Δt can be used to evaluate the short-term plasticity of artificial synaptic

devices. The double exponential function can be used to fit the relationship between PPF (PPD) index and Δt:[86]

$$\mathrm{PPF(PPD)\,decay} = C + D_1 \cdot \exp\left(-\Delta t/\tau_1\right) + D_2 \cdot \exp\left(-\Delta t/\tau_2\right) \tag{4}$$

where C is a constant, τ_1 and τ_2 are the characteristic relaxation time, t is spike interval time, D_1 and D_2 are initial facilitation magnitudes. Notably, in conventional biological synapses, the value of τ_2 is typically an order of magnitude larger than τ_1.[88-89] PPF is widely considered to play significant roles in decoding temporal information in visual and auditory signal.[89]

2.3.2. Long-term Plasticity

Long-term plasticity contains long-term potentiation/depression (LTP/LTD), which is essential for memory and learning. Compared with short-term plasticity, long-term plasticity can store external information for a longer time. As shown in Figure 2h, LTD is likely to reverse the previous LTP. Therefore, the counterbalance between LTP and LTD preserves synaptic weight in a linear range, enabling the frequency-based signals to be processed in an agile manner. The recognition accuracy of ANNs is determined by the effective multi-level states, dynamic range, symmetry and linearity of the artificial synapses weight updates.[90] The training and robustness of the ANNs can be enhanced with the increase in the effective multi-level states. The power consumption and mapping ability of artificial synapse devices are affected by the conductance (G) ranges, which is defined as the ratio of maximum conductance (G_{max}) and minimum conductance (G_{min}).[91-92] Besides, the recognition accuracy of ANNs is highly affected by the symmetry and linearity of LTP/LTD. The effective conductance states of LTP/LTD, which can be defined as the states with the overall conductance variation ($\Delta G = G_{max} - G_{min}$), is fitted by the following equations:

$$G_p = B\left(1 - e^{-n/A_p}\right) + G_{\min} \tag{5}$$

$$G_d = -B\left(1 - e^{(n-n_{\max})/A_d}\right) + G_{\max} \tag{6}$$

$$B = \frac{\left(G_{\max} - G_{\min}\right)}{\left(1 - e^{-n_{\max}/A_{p,d}}\right)} \tag{7}$$

$$AR = \frac{\max\left|G_p(n) - G_d(n)\right|}{G_p(n_{\max}) - G_d(n_{\max})} \tag{8}$$

where G_p and G_d are the conductance of potentiation and depression, respectively, n is the pulse number, and n_{max} is the maximum number of pulses, A is the linearity parameter of potentiation and depression, AR is the symmetry. An ideal synapse exhibits A = 0 and AR = 0, with a perfect symmetric conductance modulation and linearity.[86, 90]

2.3.3 SRDP and STDP

SRDP and STDP are typical long-term plasticity, which show important implications for exploring the interactions among multiple synapses.[79] They are thought to be two examples of the Hebbian learning rule. As shown in Figure 2i, SRDP indicates the dependence of synaptic plasticity on the frequency of excitation spikes, which affects brain cognitive function.[93] STDP points out that sign and magnitude of synaptic plasticity can be modified by the temporal relationship (including order and interval) between pre-synaptic signals and post-synaptic signals.[94-95] When the pre-synaptic signal precedes the post-synaptic signal, time interval (Δt) is larger than zero, and LTP occurs in synapses. Conversely, LTD is produced when the presynaptic signal follows the post-synaptic signal ($\Delta t < 0$). By changing the time intervals, a STDP curve is obtained, and the synaptic plasticity can be predicted by the STDP curve when the time interval is known. Besides, according to the STDP curve, STDP can be divided into two categories, i.e. asymmetric STDP and symmetric STDP.[96] For asymmetric STDP, the synaptic weight is determined by the time interval and the time order. As for symmetric STDP, the synaptic weight is only related to the time order.[97] Four forms of STDP, including symmetric Hebbian learning rule, symmetric anti-Hebbian learning rule, asymmetric Hebbian learning rule, and asymmetric anti-Hebbian learning rule are shown in Figure 2j. The asymmetric STDP and symmetric STDP are fitted by the following formulas, respectively:

$$\Delta w = Ae^{-\Delta t/\tau} + \Delta w_0 \quad \text{(Asymmetric STDP)} \tag{9}$$

$$\Delta w = A\exp\left(-\Delta t^2 / \tau^2\right) + \Delta w_0 \quad \text{(Symmetric STDP)} \tag{10}$$

where A is the scale factor, τ is time constant, Δt is the internal time between pre-synaptic signal and post-synaptic signal, Δw is the percentage change in synaptic weight.[98] For biological synapses, the time constants of STDP are on the order of tens of milliseconds. Adjusting the time constants of STDP are important for artificial synapses to be applied in neuromorphic systems, as various computational tasks are achieved through synapses with diverse time constants at different cortical locations or developmental stages.[99-100] The time constants of STDP can be adjusted by changing the pulse width and interval time, which have been demonstrated by Li et al.[98] Associative learning is realized by symmetric STDP, where the synaptic weights are enhanced during learning, leading to recall of original information even in incomplete or noisy situations. Sequence learning is associated with asymmetric STDP, where forthcoming events can be predicted based on the time order of previous events.[96]

2.3.4. Transition from Short-term Plasticity to Long-term Plasticity

With several iterations of external information training, short-term plasticity could be transferred to long-term plasticity. This is similar as the learning process. A simulation of the transition from short-term plasticity to long-term plasticity is illustrated in Figure 2d. According to equation (1), the decay time obtained by fitting the EPSC is associated with the memory ability. Short-term and long-term are distinguished by retention time. The timescale of short-term plasticity is typically on the millisecond to minutes, which is the physiological foundation for key computational functions in neural networks. The timescale of long-term plasticity is usually on hours or even longer, causing permanent changes, allowing the human brain to store the information.[28] Thus, the extended retention time is the sign of the transition from short-term plasticity to long-term plasticity. Spike number and spike frequency are usually used to convert short-term plasticity to long-term plasticity, which have been widely demonstrated by researchers.[75, 101-102]

2.4. Unique Characteristics of Optoelectronic Synaptic Device

Humans obtain nearly 80% external environment information through eyes.[32] Study on optoelectronic synapses is benefit for the development of neuromorphic visual systems. Optoelectronic synapses not only exhibit the above-mentioned basic synaptic functionalities, but also show some unique characteristics. For example, the synaptic plasticity of optoelectronic synapses are also dependent on the light wavelength, light intensity, and light pulse duration time. Multilevel optical memories have been realized by the optoelectronic synaptic devices, i.g. multilevel data storages were achieved by controlling the wavelength of incident light and the photonic pulse number, which show great potential for application in the logic operation and pattern recognition.[103-104] The light-wavelength-dependent plasticity enables the recognition of color-mixed patterns.[105] Besides, optoelectronic synapses are suitable for applying in optical wireless communications through the “Morse-code” decoding schemes and visual object recognitions through ANNs, which are realized by the tunability between the short-term plasticity and long-term plasticity.[104, 106]

3. Ultraviolet-Visible-Infrared Optoelectronic Synaptic Devices

The response wavelength of light is of great significance for optoelectronic device applications. Different response wavelength ranges usually have different application scenarios. For example, ultraviolet response is suitable for applying in astronomical exploration, secure communication, fire warning, high-voltage corona detection, and ozone-

hole monitoring. Jiang et al. fabricated a (Al,Ga)N ultraviolet optoelectronic devices, which showed quasi-invisible functionality to realize the 360° omnidirectional detection, and could be further applied in ultraviolet communication and astronomical exploration.[62] Visible response shows outstanding potential for application in underwater communication and artificial vision, which have been confirmed by Zhang et al. and Gu et al.[63-64] As for infrared response, it is well known that infrared range has great important applications in the military. In addition, the infrared also shows important application value in civilian, such as infrared imaging and infrared communication.[60-61] In recent years, infrared temperature measurement has played an important role in the fight against COVID-19. Besides temperature measurement, under the influence of the epidemic, the current scientific research staff is utilizing NWs materials to design and fabricate devices for their contributions against COVID-19. Wasfi et al. designed a novel Si NWs FET sensor using a semiempirical approach to detect the COVID-19 spike protein. The changes in electrical transport properties are used to illustrate the presence or absence of the COVID-19 spike protein as a target molecule. The results show that the Si NWs FET sensors have the potential to successfully detect the COVID-19 virus.[107] A ZnO NWs microplate was developed to detect the antibodies specific of asymptomatic patients with COVID-19. The ZnO NWs microplate is more sensitive than a commercial assay, which facilitate early detection of antibodies specific in asymptomatic patients with COVID-19.[108] Recently, all-in-one ZnO/In_2O_3 heterojunction artificial synapses were used to achieve COVID-19 chest image recognition by simulating artificial neural network.[109] The accuracy of the artificial synapse is 85%, which shows the potential application of ZnO/In_2O_3 heterojunction artificial synapses in ANN for COVID-19 CT image pattern recognition. Thus it is possible to use NW optoelectronic synapses to fight against COVID-19 and other viruses. If the NWs optoelectronic synaptic devices are applied in the above application fields, the information processing speed and device integration level will be improved, and the power consumption will be reduced. Thus, it is important to study NWs optoelectronic synaptic devices stimulated by different spectral range light, which lays the foundation for the application of NWs optoelectronic synaptic devices in civil and military fields. **Figure 3** shows some typical ultraviolet-visible-infrared optoelectronic materials and the band structures calculated by first-principles.[110-124] In this part, we will discuss the NWs based optoelectronic synaptic devices in different spectral range, and facilitate the future applications of NWs optoelectronic synapses.

3.1. Ultraviolet Optoelectronic Synaptic Devices

Ultraviolet light is an important observation window since the warmer an object is, the shorter the wavelengths of its radiation. The objects with the highest mass and temperature in nature are all kinds of celestial bodies, which produce a large amount of ultraviolet radiation, such as active galactic nuclei, black holes, and supernova explosions, all of which will release strong ultraviolet radiation. Besides, the large energy and strong scattering of ultraviolet make it suitable for non-line-of-sight security communication. Studying in ultraviolet optoelectronic synaptic devices is vital for artificial intelligent device for astronomical exploration and ultraviolet communication.

Ultraviolet light based synaptic devices have attracted wide attention. Gou et al. fabricated an electrical and optoelectronic SnO_2 NW synaptic transistor with a multiple in-plane gate structure, and the structure of the device is shown in **Figure 4**a.[49] Owing to the proton-related electric double-layer coupling effect, the synaptic functionalities, i.g. PPF, SRDP, and SNDP, were successfully mimicked by device triggered by electrical signal. Besides, when a 365 nm ultraviolet light is used as the light-modulating terminal, the device shows obvious photoresponse, and the EPSC is dependent on the light intensities and spike numbers, as shown in Figure 4b and 4c. Due to the rich surface states of NWs, NWs optoelectronic synapses based on trap states working mechanisms have been widely studied. A ZnO micro/nanowire photonic synapse based on piezo-phototronic effect is demonstrated in Figure 4d, whose synaptic plasticity can be successfully modulated by strains.[38] As shown in Figure 4e-i, the device exhibits light stimulated EPSC and PPF. Besides, a transition from STP to LTP is mimicked by applying repeated photonic pulses. Furthermore, the synaptic weight can be regulated by changing the light intensity and compressive strain.

In order to integrate photo-detecting and electrical processing abilities in one device, a PMMA/C8-BTBT decorated ZnO NWs p-i-n junction based synaptic transistor was demonstrated by Ni et al.[75] As shown in **Figure 5**a-d, the device shows long-term retention as long as 10^4 s. However, the above researches only discussed the optical potentiation behaviors, instead of depression behaviors. Shen et al. further designed a single ZnO NW optoelectronic synaptic device, and the device structure is shown in Figure 5e.[50] From Figure 5f-g, it is observed that the device exhibits light intensity-dependence EPSC when stimulated by ultraviolet light, and shows gate-voltage dependence IPSC when stimulated by electrical pulses in dark condition. The light triggered EPSC is owing to the light-induced O_2 desorption and the persistent photoconductivity property of the ZnO NW. In addition, the electrical pulse triggered IPSC is demonstrated by inserting a charge trapping layer. The PPF is also successfully emulated in this synaptic device. When the NW transistor is triggered by first

light stimulus, O_2 desorption will happen on the NW surface, resulting in a slow recovery process in the dark condition. Further O_2 desorption will occur and lead to a larger peak current if the second light stimulus is applied shortly after the first one. By combining electrical and optical stimuli, the synaptic weight can be modulated in the NW synaptic transistor. The reading current can be continuously increased/decreased with a set of optical /electrical pulse, as shown in Figure 5h. Additionally, the light-induced potentiation and electric field-driven depression behaviors are stable in the device. A lower power consumption of ~ 1 pJ is achieved under light pulse, indicting the application potential of NW based optoelectronic synapse with low power consumption. Besides, STDP are also investigated in this ZnO NW transistor. As illustrated in Figure 5i, with the Δt change from negative to positive, the device transfers from the LTD in the third quadrant to LTP in the first quadrant. This is a typical asymmetric Hebbian learning rule. As for the symmetric STDP (Figure 5j), with the decrease in Δt, the change of synaptic weights is increasing on both the negative and positive sides, which is similar to the autocorrelation learning behavior in the hippocampus.

In fact, the ultraviolet wavelength range also includes a vital wavelength band, i.e. solar blind, which covers the wavelength of 200 nm ~ 280 nm.[125] The sun is the most typical and powerful natural light source, and its spectrum covers the whole spectral region from extreme ultraviolet to far infrared. Atmospheric background radiation is generated by the sun in a direct or indirect way, which will bring serious background interference to the optoelectronic devices working near the ground. Compared with visible light and infrared light, solar blind ultraviolet light has obvious target characteristic, strong anti-interference ability and good selectivity, and can avoid the interference of the sun. Solar blind optoelectronic devices have important applications in the communication, missile approach warning, maritime search and rescue. Recently, with the development of unmanned aerial vehicle (UAV) technology, UAVs have begun to emerge on the battlefield. Owing to the characteristics of low-altitude flight and the unsatisfactory development of defense technology in low-altitude areas, UAVs have become a powerful weapon on the battlefield. The application of solar blind synaptic devices to low-altitude defense can improve target recognition accuracy and speed, and is more conducive to military defense. Therefore, it is significant to promote the application of solar blind optoelectronic synaptic devices in low-altitude combat and defense. Chen et al. proposed a SnO_2 NW solar blind optoelectronic synaptic transistor, which was triggered by 275 nm laser.[126] An electrolyte gel in the NW channel was adopted as the gate dielectric, as shown in **Figure 6**a. The device shows an obvious n-type semiconductor behavior. Under 275

nm illumination, the off-state current is significantly higher. Besides, the threshold voltage shifts to the left, dependent on optical power, as shown in Figure 6b-c. The attractive phenomenon is that the change in threshold voltage is different when the sweeping direction is different. The EPSC and PPF are mimicked by the SnO_2 NW optoelectronic synapse and the results are given in Figure 6d-g, in which the EPSC and PPF index are dependent on the gate bias. By changing the gate bias, a transition from short-term plasticity to long-term plasticity could be observed. The programmable persistent photoconductivity phenomenon originates from the photo-generated carriers trapped at the surface and interface between the dielectric and the NWs. The trapped carriers produce a local electric field, leading to the photogating effect.

Photogating effect can be attributed to the extension in excess carrier lifetime caused by impurities and defects or designed hybrid structures. An additional electric field that may modulate the channel conductance like the gate voltage will be generated if one type of photo-generated carriers is trapped and spatially distributed. The low-dimensional photodetectors dominated by photogating effect can exhibit high responsivity and restricted response speed due to the prolonged excess carrier lifetime. Thus, photodetectors usually require a trade-off between bandwidth and gain. As for optoelectronic synaptic devices, they need proper data retention capability, so the optoelectronic synaptic devices are not limited by the trade-off between bandwidth and gain. The gain is mainly generated by the following process: if the lifetime of excess carrier is longer than the transit time, when the excess electron reaches the anode, another electron will immediately enter the photoconductor from the cathode and drift to the anode in order to maintain charge neutrality. This process repeats until the remaining electrons recombine with holes, which directly results in a device gain greater than 1. The photogating effect can be seen as a special case of the photoconductive effect, as both have the same gain definition and need to operate with a bias. In addition, for optoelectronic devices based on p-n junction, the built-in electric field is generated at the junction area, where the photo-generated carriers can be effectively separated, also resulting in the increase in excess carrier lifetime.[127]

In the synaptic device, photogating effect not only induces a shift in threshold voltage, but also leads to a long decay time. The gate bias dependence of EPSC and PPF index can be elucidated by the energy band diagrams. The Fermi level of SnO_2 will shift down under a small negative gate bias, resulting in a slight decrease in the electron concentration, as shown in Figure 6h. The photo-generated holes and shallow donor states are trapped in the surface level, resulting in photogating effect. As the gate bias becomes more negative, the Fermi level

shifts down into the energy gap, as shown in Figure 6i. Fewer holes will be trapped at surface level, and the acceptor levels are nearly unoccupied by electrons, resulting in the weakness in photogating effect. The activity of SnO_2 optoelectronic synaptic devices triggered by solar blind ultraviolet light spikes can be used to address deep ultraviolet pollution, secure communication, military surveillance and target acquisition. However, the power consumption is hundreds of picojoules, which is much higher than that of human brains.[5-7]

The single spike power consumption (E) in the optoelectronic synaptic device can be defined as the sum of electrical power consumption (E_1) and light power consumption (E_2). The electrical power consumption is extracted by the following formula:

$$E_1 = I_{peak} \times t \times V \tag{11}$$

where I_{peak} is the peak value of EPSC triggered by a single pulse, t is the pulse duration time, and V is the applied bias voltage. The light power consumption is calculated by the following formula:

$$E_2 = P \times A \times t \tag{12}$$

where P is the input light intensity, and A is the effective area of the NWs. Actually, various methods have been adopted to calculate the power consumption of optoelectronic synaptic devices. Some researches only concerned about the light power consumption or electrical power consumption.[54, 128] In some application scenarios, such as neuromorphic visual sensors, it seems more reasonable to only concern about the electrical power consumption to evaluate the power consumption of the optoelectronic synaptic devices, which means the device is worked under the driven of electric power, and can response the external light stimuli. When NWs optoelectronic synapses are applied in neuromorphic computing, both of electrical power consumption and light power consumption should be concerned. Neuromorphic computing requires synaptic devices to couple with axon and dendrite units in ANNs. Although the power consumption of ANNs does not completely depend on synaptic devices, an optoelectronic synaptic device with low power consumption is of great significance for realizing low power consumption neuromorphic computing. According to equation (11) and (12), decreasing the driving voltage, reducing the device area, accelerating the response speed, and improving the photosensitivity of the device can significantly reduce the power consumption. The quasi-1D structure of NWs makes them show smaller effective device area and shorter photo-generated carrier transport time. The rich surface states of NWs usually lead to photoconductive gains, and the photosensitivity of NWs optoelectronic synapse can be improved. The low dimension and high light absorption of NWs make them one of the most important candidates for low power consumption optoelectronic synapses.

To decrease the power consumption, Meng et al. fabricated a quasi-two-dimensional electron gases (quasi-2DEGs) solar blind photonic synapses based on $InGaO_3(ZnO)_3$ superlattice NWs, which is shown in **Figure 7**a.[37] 261 nm UV light is used as optical stimulus. The transition behavior of short-term plasticity to long-term plasticity is mimicked by extending the spike time. More importantly, the power consumption of a single event is as low as ~ 0.7 fJ, which is lower than that of biological synapses. A comparison of power consumption of various materials based optoelectronic synaptic devices is shown in **Table 2**.[37-41, 49-50, 90, 102-103, 126, 128-143] It can be concluded that the NWs optoelectronic synaptic devices have great prospects of being applied to lower power consumption devices.

The ultralow power consumption of Meng's work is originated from the material properties and device structures. The high surface-to-volume ratio of NWs is beneficial for the adsorption-desorption of oxygen, the short channel length can decrease the energy loss, and the quasi-2DEG make high mobility NWs show high sensitivity to electrical and optical stimuli. Furthermore, PPF, light intensity-dependent plasticity, SNDP and STDP are also demonstrated. The results are shown in Figure 7c-f. The device shows a large PPF index of 210% and asymmetric STDP behaviors. The operation mechanism of the device is investigated by the schematic diagrams. In the dark, the free electrons in the NW core are captured by the oxygen molecules adsorbed onto the surface of NW, and oxygen ions with negatively charged are produced. At the same time, the free electrons in the NW core will be depleted, resulting in a decrease in the conductivity. An additional electrostatic field will be induced by the trapped carriers onto the NW surface, and the channel conductance can be modified by the electrostatic field. As the device exposures under UV light, a large number of photo-generated carriers are generated. These holes migrating to NW surfaces will recombine with the surface electrons, leading to a release of the adsorbed oxygen ions. Meanwhile, the conductivity of quasi-2DEGs is significantly improved owing to the collection of photo-generated electrons in the multiple quantum wells. Once the UV light is turned off, the hetero-interface barriers between InO_2^- and $GaO(ZnO)_3^+$ result in the spatially separated photo-generated carriers, and prevent the photo-generated electrons diffusing to NW surfaces. A longer delay time is caused by the localized electrons, leading to the synaptic plasticity in quasi-2DEGs photonic synaptic devices. This 2DEG NW device can significantly reduce power consumption and improve sensitivity, and show promising applications in the development of neuromorphic devices.

In conclusion, ultraviolet NWs optoelectronic synaptic devices have received widespread attentions. Until now, researches of NWs ultraviolet optoelectronic synaptic devices focus on

basic functionalities of synaptic devices. Further promoting the application of NWs ultraviolet photoelectric synapses in ANNs is urgent and of great significance for astronomical exploration and ultraviolet communication.

3.2. Visible Optoelectronic Synaptic Devices

Visible range is the portion of the spectrum that is visible to the human eyes, which make visible optoelectronic synaptic device suitable for artificial vision. Besides, since the seawater possess a low attenuation of light waves in 450 to 550 nm range,[144-146] visible optoelectronic devices can be used in high-speed underwater wireless optical communication. This technology has the advantages of low latency and high security, and is thought as a vital alternative candidate for underwater communication.[147] In addition, underwater wireless optical communication can also be applied to marine exploration, such as environmental monitoring and marine resource exploration[144, 147-148] Applying visible light optoelectronic synaptic devices to underwater wireless optical communication can effectively improve the speed and safety of information processing, and reduce power consumption. Consequently, it is important to develop visible optoelectronic synaptic devices.

O'Kelly et al. preformed a TiO_2 NW visible optoelectronic synaptic device with Au contacted, which is shown in **Figure 8**a.[130] The device displays evolving conductance states with repeated voltage pulse stimulus, which is similar as a memristor. As shown in Figure 8b, the device response to 405 nm visible illumination, and the photocurrent is increased linearly with voltage and then reached saturation. Voltage stimuli and optical pulses, including uncorrelated and coincident, are performed to trigger the device, and the results are shown in Figure 8c. Both of uncorrelated voltage and optical pulse can produce modest response, when the voltage and optical pulse are coincident, an exceptional response is observed which is distinctly higher than the sum of the uncorrelated pulses responses. The dependence of current enhancements on the time and the number of the pulse stimuli is also proposed. Figure 8d shows the plot of the current enhancements versus pulse time interval. The curve is mirrored through $\Delta t = 0$, indicating that the current augmentation is not dependent on the sequence of the stimuli. This phenomenon is analogous to the STDP in biological systems. The device response to different numbers of optical, voltage, and coincident pulses are explored in Figure 8e. An enhancement in uncorrelated and coincident response is observed with the increase in test cycle number, which is similar to neural short-term plasticity. This is related to the property of TiO_2 and its matter interaction with light. Owing to the Schottky barrier between the TiO_2 and Au, the conduction band will bend upward and a depletion region is formed. The

oxygen vacancy generation and O_2 adsorption of the NW can further modulate the Schottky barrier height. Under positive bias, oxygen vacancies are formed at the TiO_2-Au interface, and the electrons release into conduction band. The electrons will reduce the depletion region width and increase the current. Besides, the O_2 in the ambient will react with the conduction band electrons, leading to the adsorption of O^{2-}, and generate an additional Schottky barrier at the contact area. Under illumination, the photo-generated holes are driven to the interface by the upward band bending, resulting in desorption of O^{2-}. Most of the liberated O_2 remain trapped at the Au-TiO_2 interface, and further recombine with photo-generated electrons. When the applied bias is larger, the recombination process will be inhibited, causing the increased conductivity for a short time. The learning process arises from the steady accumulation of photo-generated carriers due to repeated coincident stimuli.

An InAs NW phototransistor covered with a native oxide layer was proposed by Li et al. as illustrated in Figure 8f.[132] The 532 nm laser pulses are acted as the pre-synaptic spikes, and the drain current and the channel conductance of the transistor are regarded as the post-synaptic current and synaptic weight, respectively. In contrast to the above researches, the drain current of this device becomes lower under illumination, as shown in Figure 8g. This is a typical negative photoconductivity, which can be explained by photogating effect.

The positive and negative photoconductive responses of NWs are related to the trap states on the NWs surfaces and the conductivities inside the NWs.[149] Under the illumination of light with suitable photon energy, NWs will absorb photons and produce photo-generated electron-hole pairs. When the conductivity inside the NWs is small, one type of photo-generated carriers, i.g. photo-generated electrons in N-type NWs, will transport to the NWs surface and be trapped by the surface states. At the same time, the photo-generated holes will recombine with the free electrons inside the NWs. Since the free carrier concentration inside the NWs is small, the photo-generated holes will increase the carrier concentration inside the NWs, result in positive photoconductive responses. When the conductivity inside the NWs is large, after the photo-generated holes recombine with the free electrons inside the NWs, the remained photo-generated holes concentration is not enough to make the conductivity higher than that in dark, leading to negative photoconductive responses.[58, 132, 149] The positive and negative photoconductive responses of NWs can be further adjusted by the surface states density, intrinsic carrier concentration, light intensity, and light wavelength.[59, 150-153] Here, we list some typical NWs materials that exhibit positive or negative photoconductivity responses in **Table 3**.[39, 59, 75-76, 102, 149, 154-165]

As shown in Figure 8h, a native oxide layer, i.e. photogating layer, is existed on the surface of InAs NWs. The photo-generated electrons of the InAs NW are either trapped by the photogating layer or recombine with the holes after thermalization. Owing to the high mobility of InAs NWs (1448 $cm^2 \cdot V^{-1} \cdot s^{-1}$), the hot electron mean free path of InAs NW is long, which increase the hot electron trapping possibility of photogating layer.[150] Photo-generated electrons are trapped by photogating layer, and the photo-generated holes are recombined with channel electrons, leading to a decrease in the drain current. The negative photoconductivity effect is related with the illumination intensity. When the illumination intensity is high enough, photogating effect will no longer dominate the entire photoresponse process, leading to the disappearance of the negative photoconductivity effect. The synaptic plasticity, including STP, LTP and PPF are effectively mimicked by the device. Figure 8i shows the dependence of retention time and light power intensity. The retention time is positively correlated with light intensity. A transition from STP to LTP is realized by increasing the light intensity. When the device is triggered by low intensity light spikes, the post-synaptic current recovers to the original state rapidly. When the light intensity is high enough, the recovery time of post-synaptic current is slow. All these synaptic behaviors can be explained by the photo-generated electrons trapping/detrapping in the photogating layer.

Zha et al. further studied the optoelectronic synaptic behaviors of InAs NW phototransistor.[131] The device displays negative photoresponse when the incident light intensity is lower. When the light intensity exceeds 1 W/cm^2, the device shows positive photoresponse instead. The negative photoresponse is induced by photogating effect. When the energy of photo-generated hot electrons in InAs NWs is higher than the trap barrier height in the gate control layer, the interface traps will capture photo-generated electrons before thermalization back to the conduction band, resulting in the participation of conduction band electrons in the recombination. Then the conduction band electron density is reduced and the response current is decreased, produced a negative photoresponse. When the light intensity is high enough, the number of photo-generated electron-hole pairs will increase, and the negative photoresponse no longer dominate in whole optical response. The synaptic functions, such as STP, LTP, PPF, are mimicked in the device by utilizing the negative photoconductive effect. Besides, the transition from STP to LTP can be realized by adjusting the gate voltage. The photoresponse behaviors can also be adjusted by traps concentration. Negative photoresponse is no longer dominated when the traps concentration is low enough. Tuning photoresponse behaviors is beneficial for realizing all-optical-controlled devices.

Li et al. proposed a CMOS-compatible selective-assembling porphyrin Si NWs transistor, which combined the high photo-sensitivity of porphyrin and low dimensional transport features of Si NW.[102] The schematic diagram of the device is demonstrated in **Figure 9**a. Both n-type and p-type Si NWs are investigated. As depicted in Figure 9b-c, n-type Si NWs show negative photoresponses, conversely, p-type Si NWs show positive photoresponses. These phenomena are similar to the IPSC and EPSC of biological synapses. A simple physical model is established based on energy band bending effects, which is shown in Figure 9d. In dark, as the energy bands of Si NWs surface and chromophore are different, the conduction band will bend and cause a small positive shift in transfer curve. Under illumination, a lot of photo-generated carriers are produced, porphyrin molecules accept electrons from the Si NW conductance band, and the electron transfer process will generate an additional negative electric field, which makes the conductance band bend upward. Thus, the n-type channel carriers are depleted and the drain-source current is reduced. After removing the illumination, the captured electrons in porphyrin will gradually release to Si NWs via thermal emission, leading to the increase in drain-source current. As for p-type Si NWs device, the electron transfer process will increase the number of p-type channel carriers, resulting in the enhancement in channel current. Based on this physical mechanism, the PPD and PPF are performed as shown in Figure 9e-f. The n-type Si NWs synaptic devices show PPD behavior when stimulated by a pair of light pulses, while p-type Si NWs synaptic devices show PPD behavior. The function between PPD index and optical pulse interval is measured and fitted by equation (4). The relaxation time scales are analogous to the rapid and slow transitions in biological synapses.[28] Figure 9g shows the light frequency-dependence plasticity of n-type Si NWs synaptic devices, which is suitable for high-pass filter.

Visible optoelectronic synapses have been studied to mimic the basic synaptic functionalities. Positive and negative photoconductivity effects have been found in NWs, which means that NWs have application prospects in all-optical-controlled synaptic devices. Research on visible optoelectronic synaptic devices can lead to important implications for artificial vision systems and underwater optical communication.

3.3. Infrared Optoelectronic Synaptic Devices

Infrared devices have great important applications in civilian and military, including infrared imaging, infrared communication, infrared temperature measurement, and infrared air defense weapon.[60-61] For human eyes, irreversible damage on the retina and lens can be caused by short-wavelength infrared light.[166] Broadening the light response range of synaptic devices is

very important. In modern warfare, to achieve efficient damage, it is necessary to use different fire interception methods for different air targets, or calculate the attack and escape areas according to the types of targets. Therefore, air target recognition is one of the indispensable capabilities of air defense weapons. Infrared neuromorphic devices can effectively detect and identify air targets, which have the advantages of all-weather use, good concealment, wide detection range, high positioning accuracy, strong identification and camouflage ability, long penetration distance, etc. Moreover, they will not actively emit signals and expose their own position during detection. The study of NWs infrared optoelectronic synaptic devices could efficiently improve the speed and accuracy of target recognition, which is more conducive to attack and escape, and is beneficial to the preparation of low-power civilian infrared imaging systems and military target recognition systems. To develop near-infrared NWs optoelectronic synaptic devices, researchers can select NWs materials with the band gap located in the near infrared spectral range, such as Si NWs, GaAs NWs and some alloy NWs.

A vertical organic field effect transistor with Ag NWs/PCDTPT film was proposed, and the floating-gate layer is composed of CdSe/ZnS quantum dots/PMMA composites, which is shown in **Figure 10**a.[103] As seen in Figure 10b, the device exhibits a typical p-type semiconductor behavior. For floating-gate transistors, the transfer curve hysteresis and the shift of threshold voltages are usually used to investigate the data storage capability. When the device is programmed by different gate voltages, the hysteresis of the transfer curves and memory windows become larger with the increased programming gate voltages, which means the number of trapped carriers in floating-gate is augmented. When the device is programmed by light stimuli with different wavelengths, including visible to near infrared, a lot of photo-generated carriers are produced. The drain current of the device becomes larger and the threshold voltage is shifted positively, and the results are shown in Figure 10c. Under the excitation of 830 nm light, the shift in threshold voltage is the largest, which is corresponding to the absorption peak of PCDTPT. It indicates that the shift in threshold in related to the photo-generated carriers number. The change in threshold voltage is caused by the charges captured by the floating-gate. More photo-generated carriers are produced in the PCDTPT, and more charges are trapped by floating-gate. Furthermore, due to the different sensitivities of the vertical organic field effect transistor to diverse incident light, a wide range of photocurrent currents can be achieved, and multiple memory states can be distinguished. It means that the device have the capability of multi-level data storage. The variation of the storage window with time at different wavelengths is performed to measure the retention property of the device. As shown in Figure 10d, six-level current state is observed, and the

retention current state of the device is not significantly degraded after 10000 s. Besides, the device also exhibits stable storage performance, the current state remains stable after 200 cycles. This transistor has great potential for application in memory devices.

An artificial synaptic device based on ferroelectric P(VDF-TrFE) wrapped InGaAs NW was designed by Xie et al.[39] Schematic diagram of the artificial synaptic device is shown in Figure 10e. Owing to the negative photoconductivity of NWs, the device can realize LTP/LTD through electrical and 450 nm light stimuli, respectively. As demonstrated in Figure 10f, 100 electrical excitatory spikes and 100 visible light inhibitory spikes are applied to the InGaAs NW artificial synaptic device. The nonlinearity parameter is also extracted, which demonstrates that the thickness of ferroelectric P(VDF-TrFE) will influence the nonlinearity parameter. The thicker ferroelectric P(VDF-TrFE) can introduce more ferroelectric domains. The polarization electric field intensity generated by the thicker ferroelectric P(VDF-TrFE) is easier to change linearly when the continuous pulse intensity is a constant. The LTD nonlinearity parameter of the device with 450 nm light pulses is notably lower than that with electrical pulses. LTP and LTD are critical for enabling low-power computing. When the nonlinearity is lower, the computational accuracy will be better. In addition, the negative photoconductivity is dependent on light wavelength, and a shorter wavelength is easier to induce the negative photoconductivity behavior. The device expresses positive photoconductive behavior under 1550 nm infrared illumination. Concerned about this, electrical and infrared pulses can be used to achieve the associative learning.

Lee et al. proposed a NW optoelectronic sensorimotor synapse, which is realized by combining an ion gel-gated electrochemical organic NW transistor and a photodetector.[167] As shown in **Figure 11**a, the biological synapses in the sensorimotor nervous system are simulated by the NW transistor based artificial synapses. The EPSC and PPF are successfully mimicked by the transistor when triggered by gate voltage as shown in Figure 11b. The negative pre-synaptic voltage spikes can attract anions to accumulate near the NW surface, leading to a hole transport channel in the NW. EPSC is generated under the driving of voltage. The PPF is caused by the accumulation of additional anions in the second pulse before the accumulated anions during the first pulse are fully diffused. The device is also stable under strains. As for the optoelectronic synapse, the photograph and structure of the device is shown in Figure 11c-d. The EPSC and PPF are generated by light-induced voltage spike from photodetector under illumination. The organic NW optoelectronic transistor can response to patterns of ultraviolet-visible-infrared light that denote the International Morse code, where the English letter can result in a distinct EPSC amplitude response. Each letter is linearly

related with the sum of EPSC amplitude peak values. For example, the standard emergency signal “SOS” is successful responded by the organic NW synaptic transistor under visible light illumination when the stains is 0 and 100%, as shown in Figure 11e. The device can also respond the short messages of “HELLO” and “UNIVERSE” under 940 nm and 365 nm light, and the results are shown in Figure 11f. All these results demonstrate the application potential of this device in optical wireless communication.

Although infrared optoelectronic synaptic devices based on NWs have been developed, current research lacks all-in-one infrared NW optoelectronic synaptic devices and NW optoelectronic synapses with near-band-edge response. To improve the application potential of NWs infrared optoelectronic synaptic device in civilian and military, a device that integrates sensing, storage and computing is needed. The photoelectric conversion process in optoelectronic device mainly includes the generation-separation-transport-collection of photo-generated carriers. When the excitation photon energy is much larger than the bandgap of the material, the photo-generated electrons will transfer to a higher energy state above the bottom of the conduction band. Such photo-generated electrons are more likely to scatter and collide compared with that excited by the photon whose wavelength is near the band edge of the material. Thus, the near-band-edge response NW optoelectronic synapses usually show higher sensitivity. It is important to develop NW optoelectronic synapses with near-band-edge response.

4. Neuromorphic Applications

NW optoelectronic synaptic devices are triggered by optical stimuli, which provide a noncontact way to mimic biological synaptic functionalities, and promote the development of highly intelligent neuromorphic devices. Apart from the basic synaptic functionalities described in part III, such as EPSC, PPF/PPD, LTP/LTD, SRDP, and STDP, building a bridge between optoelectronic synaptic devices and neuromorphic applications is extremely important. In this part, we review the recent advanced neuromorphic applications based on NW optoelectronic synaptic devices, including neuromorphic visual sensors, logic operation, pattern recognition, and associative learning, which is beneficial for readers to further understand and promote the development of NW optoelectronic synaptic devices in future neuromorphic applications.

4.1. Neuromorphic Visual Sensors

Human eye is a complex visual system that generates visual information by perceiving light signals. Humans obtain nearly 80% external environment information through eyes.[32] The visual pathway consists of retina circuitry, optic nerves, and visual cortex. First, the optical signals are sensed by retina circuitry, the photoreceptor cells translate light signals into electrical signals, and the electrical signals are transmitted to other retina cells for preliminary information integration processing. Subsequently, various retina cells transmit the integrated signals to the ganglion cells, and further to the brain through the optic nerve. The signals are further integrated and processed through the lateral geniculate body and transmitted to the primary visual cortex after the visual information enters the brain. The key features of visual information are extracted by primary visual cortex and further transmitted to advanced visual cortex. The advanced visual cortex performs final processing on visual signals, such as detecting motion, detecting shapes, and recognizing patterns. Finally, the results are transmitted to other brain areas, thereby affecting human behavior and thinking.[30]

To mimic the human vision, photodetectors, storage units and processing units should be integrated in artificial visual systems. However, traditional artificial visual systems face the challenge of separating storage units and processing units, which brings the problem of high-power consumption. Neuromorphic visual systems based on optoelectronic synaptic devices are proposed to solve this problem. Research on optoelectronic synaptic devices with broad-spectrum response, high light sensitivity, adaptive light intensity, and following learning rules are of great significance for the development of neuromorphic vision. NW optoelectronic synaptic devices show outstanding potential for application in neuromorphic vision.

It is well known that the primary visual cortex has the functions of orientation selectivity, which is extremely important for visual image encoding.[168] Since the feed-forward filtering function of primary visual cortex can lead to the increase in the weight near the particular orientation, neurons are more likely to respond to the edges with a particular orientation of input images. An orientation dependence experiment based on $InGaO_3(ZnO)_3$ NWs photonic synapses is performed to mimic the orientation selectivity in the primary visual cortex.[37] **Figure 12**a shows the schematic diagram of the human visual system. As shown in Figure 12b, a square panel with grating patterns is placed vertically between the incident light and the device, which is moved laterally under control with a fixed speed. Incident light is irradiated on the device through the square panel. In addition to moving laterally, the grating patterns can also rotate with different orientation angles. The orientation angle is defined as 0° when the grating patterns are perpendicular to the incident light. When the grating patterns are rotated in a clockwise direction, the orientation angle becomes larger, otherwise, the

orientation angle becomes smaller. During the lateral movement, the presynaptic terminal of the $InGaO_3(ZnO)_3$ superlattice NWs photonic synapse will receive the optical signal which is passing through the edge of the grating patterns.

The maximum EPSC peak at each orientation angle is defined as the visual response. Ten continuous optical pulses were used to trigger the device. The dependence of visual response and orientation angle is illustrated in Figure 12c. When the orientation angle is 0°, the maximum EPSC peak induced by 10 successfully consecutive optical pulses is 6.47 μA. It is found that only four optical pulses can trigger the device when the orientation angle is changed to 72°, and the maximum EPSC peak is 2.55 μA. According to typical neuroscience protocols,[169] the criterion of orientation selectivity is determined by half-maximum height of the fitted curve, which is 45° in this work. This value is comparable to the visual cortex of monkeys in biological experiments.[170] The devices array is fabricated to mimic artificial visual system, which can be used to record the optical information of the applied human hair pattern light, as depicted in Figure 12d. In this case, only the devices exposed to patterned light is triggered. Thus, a hair-shaped pattern is observed in the EPSC of the device array after turning off the light, as shown in Figure 12e. Besides, the device array exhibits pattern storage capability. The hair-shaped pattern can still be observed after 1 hour. The device has successfully integrated detectors, storage units and processing units, and is of great importance for neuromorphic visual hardware applications.

Kumar et al. performed a self-adaptive angular visual perception system based on Ag NW/TiO_2 Schottky optoelectronic synaptic device.[106] Schematic diagram of the Ag NW/TiO_2 optoelectronic synaptic device is shown in Figure 12g, where driven voltage is applied onto Ag NWs, and FTO is kept as grounded. The device can not only mimic artificial synaptic functionalities, i.g. PPF, PPD, and transition from STP to LTP, but also sense a broad angular view. The mechanism of these synaptic functionalities can be explained by band alignment. When the device is stimulated by positive voltage, drift electrons in TiO_2 are trapped in defects at the Ag NWs/TiO_2 junction. Under illumination, photo-generated carriers are produced, which can also be trapped by the interfacial defects. This process will enhance the learning process under applied positive electrical spikes. Specifically, the trapped electrons can be neutralized by applying negative electrical spikes. In addition, the angular sensitivity of the device is derived from the dependence of the light sensitivity on the illumination angle. As demonstrated in Figure 12h, when the illumination angle increases from 0 to 70°, the light sensitivity decreases gradually. This may be originated from the changed effective illumination area with the change of illumination angle, demonstrating that

the sensing device possesses a broad angular view. The device is further proposed to mimic biological visual perception. A 3 × 3 device array is fabricated and the device array is performed to mimic the angular spatiotemporal visual perception system. The dynamic response of the device array is dependent on the light intensity, illumination angle and the number of light spikes. Figure 12i shows the optoelectronic coupling dependent memorization behavior of the device array. When the device array is trigged by single electrical pulses, it shows the learning behavior (Bottom of Figure 12i), which is enhanced and dependent on the incidence angles. Two different input patterns, "C" and "T", are recognized by the device array (Top of Figure 12i), which confirms that the Ag NW/TiO_2 Schottky optoelectronic synaptic device array shows great potential for broad angular visual perception.

4.2. Logic Operation

Logical functions are fundamental elements of computation. Realization of logic operation function through optoelectronic synaptic device is advantageous for processing information. Numerous logical functions, such as OR, AND, NAND, and NOR, have been realized by optoelectronic synaptic devices.[26, 171-172] NW optoelectronic synaptic devices have also been investigated to realize logic functions.

Wu et al. have realized logic gate with "AND" and "OR" operations by Ag NWs/PCDTPT film floating-gate transistor, and further analyzed the application of logic gate in image processing and cognition.[103] The operation state is controlled by two light beams. Besides, gate voltage is used for programming and erasing. The current dependent on the operating sequence of two light signals and gate voltage is shown in **Figure 13**a, and the wavelengths of the light signals are 415 nm and 755 nm. When the input light is turned on, it is determined as logical 1, otherwise is determined as logical 0. As for the output signals, when the current is higher than 1.5 mA/cm^2, the device outputs logical 1, else outputs 0. When the input signals is the illumination of 415 nm and a gate voltage of +40 V, which is shown in Figure 13b, logic gate "AND" is realized. The inset is the schematic diagram of the switching of logic operation under diverse wavelengths. When the illumination wavelength is changed to 755 nm, the logical function of "OR" is obtained, as shown in Figure 13c. A device array was fabricated to further analyze the application of logic gate in image processing and storage capability. Figure 13d-i illustrates the image processing and memorizing behaviors of the device array, and different images are recognized by the device array with different wavelength of light, indicating that different logic functions is implemented. Besides, the recognized image can still be hold after one day owing to the excellent information storage capability of the device.

This work indicates that NW optoelectronic synaptic devices show great potential in logic operation.

4.3. Pattern Recognition

Pattern recognition is an important neuromorphic application for optoelectronic synaptic devices, which is necessary to promote the progress of brain-inspired neuromorphic computing.[173] Pattern recognition refers to the ability to identify typical features in digital images. High accuracy and integration are required in pattern recognition technology.

Xie and co-workers proposed P(VDF-TrFE) wrapped InGaAs NW synaptic transistors to simulate the supervised learning behavior based on the MNIST database, as shown in **Figure 14**a.[39] They perform a single layer perceptron artificial neural network (ANN), which contains 784 input neurons and 10 output neurons. The schematic diagram is provided in Figure 14b, where the input neurons are matched with the 28 × 28 pixels of the MNIST image data, and the output neurons are corresponding to 10 digits, i.e. 0 to 9. The training process adopts a unidirectional update algorithm, and the training results are shown in Figure 14c. It is obviously that the accuracy of training is related to the P(VDF-TrFE) thickness and the way of training. A proper P(VDF-TrFE) thickness and training method make the accuracy of the device reaches over 80% in fewer training times, which can greatly reduce the power consumption of the neuromorphic system. The results indicate that NW synaptic transistor show great application potential in neuromorphic computing. However, the accuracy still needs to be improved.

A ZnO NW optoelectronic synaptic transistor was further demonstrated to simulate ANN, which was applied to image recognition.[50] According to MATLAB simulation, supervised learning is realized by a three-layer perception neural model with back propagation algorithm. As shown in Figure 14d, the handwritten digits obtained from the MNIST database are divided into 16×16 pixels, which are equivalent to 256 input neurons. After preliminary processing, the input information is transmitted to the hidden neurons for further processing. Finally, the results are generated by output neurons, which can output 10 digits from 0 to 9, respectively. The recognition results are shown in Figure 14e. Besides, the recognition rate reaches 92% after 20 training epochs.

4.4. Associative Learning

Associative learning refers to the learning process realized by the connection between two or more stimuli-induced central excitations in the human brains. It means that through repeated

paired stimuli, an association will be formed between conditioned stimuli and unconditioned stimuli, i.e. classical conditioning reflex and operant conditioning reflex. Pavlov's dog experiment is a typical example of classical conditioning reflex which can be realized by optoelectronic synaptic devices. Feeding food and bells were chosen as unconditioned stimuli and conditioned stimuli for salivation. Initially, only feeding food activates the unconditioned response, i.e. salivation. Through repeated training, after the bell and feeding were associated, the bell alone could induce a conditioned response to salivation. It shows that conditioned response can be obtained through associative learning.

The classical Pavlov conditioning was demonstrated by SnO_2 NW photo-synapses.[126] As the optical stimulated EPSC is larger than the electrical stimulated EPSC, optical stimulus is concerned as an unconditioned stimulus, i.e. food, resulting in an unconscious or procedural memory. When the device is triggered by optical spikes, an unconditioned response, i.e. salivation, will be produced. Electrical pulses are considered as the bell, which is a conditioned stimulus. A threshold of 150 nA is defined to distinguish whether the synaptic device produces a salivation response. Firstly, the bell ring is simulated with 20 electrical spikes. As shown in **Figure 15**a, it can be seen that the EPSC is lower than the threshold after the simulation of bell ring, thus no salivation response is induced. On the contrary, when the device is triggered by 20 optical spikes, the EPSC is larger than the threshold, so the salivation response is produced, as shown in Figure 15b. Nevertheless, following simultaneous stimulation with food and bell ringing, EPSCs increase above the threshold, causing salivation, and the result is shown in Figure 15c. The associative reflex is established between unconditioned stimuli and conditioned stimuli after repeated training. Then EPSC above the salivation threshold can be induced by the electrical spikes as well (Figure 15d). This associative reflex can be continued for a long time, and then this connection will be forgotten over time to reduce the redundant information stored in biological nervous systems. The authors observe the forgetting behavior in the device, which is shown in Figure 15e, and after 1 h the associative reflex is disappeared. However, such associative reflex can be re-established by relearning with fewer training. As demonstrated in Figure 15f, the EPSC is increased above the threshold with electrical spikes, induced salivation response.

Xie et al. have also performed a ferroelectric P(VDF-TrFE) wrapped InGaAs NW artificial synaptic device to mimic Pavlovian conditioning, where electrical spikes are used as unconditioned stimulus, and infrared spikes are adopted as conditioned stimulus.[39] When the bell ring is simulated by infrared pulses, the EPSC is lower than the salivation threshold, and the salivation response is not produced. After training with bell and food, the EPSCs increase

above the salivation threshold, resulting in salivation response after the dog hearing the ring. When stimulated with single food, EPSC will come back to the same level as the final training after a short period of time. In addition, mixed stimulation can be adopted again to strengthen the association of unconditioned stimulus and conditioned stimulus. Kumar et al. mimicked classical Pavlovian conditioning by purely photonic pulses.[129] The bell ring is mimicked by three UV illumination photonic pulses, and food is mimicked by twelve UV illumination photonic pulses. When training with bell and food, the EPSC is higher than the salivation threshold with long retention time, which can be explained that the number of photo-generated electron hole pairs is entirely depending on the illumination time. After training, only bell ring can generate current above the threshold value to salivation.

Operant conditioning reflex also belongs to the associative learning, which can be realized by Skinner box. It means that people create a problem for the animal and observe how the animals solve the problem. However, operant conditioning reflex mimicked by NW optoelectronic synapses has been rarely studied. Ni et al. investigated a ZnO NW-based neuromorphic transistor to mimic the release of dopamine and noradrenaline in Skinner box experiment by regulating the external stimulation and internal environment.[75] For the device, the external stimulation is the gate bias, and the internal environment is the drain voltage. The electrons transmitted under a positive drain potential is similar as the release of dopamines, and the electrons transmitted under the negative drain potential is defined as the release of noradrenalines. Besides, the EPSC is induced by positive gate spikes, in contrast, negative gate spikes can lead to IPSC. An approach-avoidance behavior (AAB) threshold is defined as ±100 μA. Initially, dopamine plays a dominant role in the process of rat exploring electrified cage. When the rat contact with the electrified cage for the first time, i.e. the device is triggered by positive gate bias, the dopamine-induced EPSC will decay rapidly below AAB threshold, thus the AAB is not produced. However, the rat exploring electrified cage process will be dominated by noradrenaline. Then the rat is contacted with the electrified cage again, and the noradrenaline-induced EPSC is higher than the AAB threshold and retains for a long period. Under this circumstance, the rat fears the cage and stays away from it. The positive gate bias is used to trigger the device, which is similar as a cheese near the cage, the EPSC will be weaken (below the AAB threshold), and thereby the rat no longer fears the electrified cage. The AAB is beneficial for human to avoid the external harm. Although the operant conditioning reflex is not triggered by light, the results provide a reference for future optoelectronic synapse-based operant conditioning reflex.

5. Conclusions and Challenges

In summary, we have introduced the recent process of NWs-based ultraviolet-visible-infrared optoelectronic synaptic devices, and further discussed the application of the devices in neuromorphic optoelectronic systems. Since the application scenarios of the device are dependent on the response wavelength range, we have introduced different response wavelength ranges, which provide a reference for future applications of NWs-based optoelectronic synapses. To meet the requirements of diverse application, various NWs materials have been designed to mimic optoelectronic synaptic functionalities in different light wavelength ranges. Due to the rich surface states of NWs, the working mechanisms of most NWs based optoelectronic synaptic devices rely on trap states. For instance, through the oxygen adsorption/desorption processes in oxide NWs, NWs optoelectronic synapses with optical facilitation and electrical inhibition can be realized. To explore all-optical-controlled synaptic devices, negative photoconductive devices need to be developed. The electrical facilitation and optical inhibition NWs synapses can be realized through the capture of photo-generated carriers by photogating layers. Then, band engineering may further optimize the device performance. An ultralow-power consumption NW optoelectronic synapse has been realized by designing of superlattice NW structure.[37] The advanced neuromorphic applications of NWs optoelectronic synaptic devices are also proposed. It is clear that NWs-based optoelectronic synaptic devices have potential advantages in achieving device miniaturization, low power consumption, and CMOS integration. NWs based optoelectronic synaptic devices have application potential in neuromorphic visual sensors, logic operation, pattern recognition, and associative learning.

NWs optoelectronic synaptic devices still face some challenges. 1) Uniform, stable, and controllable NWs arrays are required. 2) Although NWs ultraviolet-visible-infrared optoelectronic synapses have been proven to be applied in simulating synaptic functionalities and neuromorphic applications, most researches are still limited in single-device level. Future NWs-based optoelectronic synaptic devices need to have the functions of sensing, memory and computing, and should be further integrated in arrays to enable system-level neuromorphic application. 3) The number of neurons and synapses in biological neurons are as high as ~ 10^{11} and ~ 10^{15}, respectively. Achieving the interconnection of neuromorphic devices is an enormous challenge. 4) It is necessary to bring the NWs optoelectronic neuromorphic platform out of the laboratory.

The advantages, current status and future directions of NWs optoelectronic synaptic devices have been concluded in Figure 16. Future research should focus on the growth of uniform and

stable NWs, preparation of all-optical-controlled synaptic devices, further reduction of the power consumption, and fabrication of all-in-one optoelectronic synapses. Future large scale neuromorphic computing needs uniform, stable, and controllable NWs arrays. 1) By controlling the growth conditions, growth of uniform and stable NWs is possible.[174] Highly aligned large-scale NWs arrays can be assembled by a nanoscale combing technique.[175] NWs bridged channels have been studied to avoid cross-talk problem.[176] 2) All-optical-controlled optoelectronic synapses are beneficial for realizing optical wireless communication. Several materials have demonstrated positive and negative photoresponse,[39, 131] which are most realized by trap states. The rich surface states of NWs make them show great potential for applications in all-optical-controlled optoelectronic synapses. Besides, all-optical-controlled optoelectronic synapses can also be realized by designing device structures.[177] 3) To reduce power consumption, self-powered NW optoelectronic synapse is a good choice. Further increase the photosensitivity of NW optoelectronic synapse is also needed, such as surface plasmon enhancement[178] and preparation of heterojunctions[75] or complex structures by band engineering.[78] 4) The photoelectronic integration can be more effectively by fabrication of electric-double-layer biopolymer electrolyte gate.[133] Nanomanipulation provides a potential method to integrate NWs on silicon chip.[179] The near-band-edge response NW optoelectronic synapse usually shows a higher sensitivity. It is important to develop NW optoelectronic synapses with near-band-edge response. Besides, extending the wavelengths beyond 1 μm could better facilitate optical transmission in integrated systems[180] Infrared NWs optoelectronics synaptic devices need further investigation. Research on NWs materials with the narrow band gap located in the infrared spectral range is a good choice. Besides, construction of the type-II heterojunction can extend the response spectral range to near infrared via interlayer transitions.[181-182] Through the integration of system-level all-in-one NWs optoelectronics synapses, the realization of neuromorphic computing based on NWs will not be far away.

Acknowledgements

We acknowledge grants from the National Natural Science Foundation of China (Grant Nos. 61974093 and 62074104), the Science and Technology Innovation Commission of Shenzhen (Grant Nos. RCYX20200714114524157), and NTUT-SZU Joint Research Program.

Received: ((will be filled in by the editorial staff))
Revised: ((will be filled in by the editorial staff))
Published online: ((will be filled in by the editorial staff))

References

[1] A. M. Paul, V. A. John, R. A. Icaza, S. C. Andrew, J. Sawada, F. Akopyan, L. J. Bryan, N. Imam, C. Guo, Y. Nakamura, B. Brezzo, I. Vo, K. E. Steven, R. Appuswamy, B. Taba, A. Amir, D. F. Myron, P. R. William, R. Manohar, S. M. Dharmendra, *Science* **2014**, *345*, 668.

[2] M. A. Zidan, J. P. Strachan, W. D. Lu, *Nat. Electron.* **2018**, *1*, 22.

[3] C. Liu, X. Yan, X. Song, S. Ding, D. W. Zhang, P. Zhou, *Nat. Nanotechnol.* **2018**, *13*, 404.

[4] S. Manipatruni, D. E. Nikonov, I. A. Young, *Nat. Phys.* **2018**, *14*, 338.

[5] R. Yang, H. M. Huang, X. Guo, *Adv. Electron. Mater.* **2019**, *5*, 1900287.

[6] Y. V. D. Burgt, E. Lubberman, E. J. Fuller, S. T. Keene, G. C. Faria, S. Agarwal, M. J. Marinella, A. A. Talin, A. Salleo, *Nat. Mater.* **2017**, *16*, 414.

[7] L. S. Michael, A. D. Christine, E. R. Stephen, B. Baek, R. P. Matthew, F. H. Peter, D. D. Paul, P. B. Samuel, H. R. William, *Sci. Adv.* **2018**, *4*, e1701329.

[8] L. Sun, Y. Zhang, G. Hwang, J. Jiang, D. Kim, Y. A. Eshete, R. Zhao, H. Yang, *Nano Lett.* **2018**, *18*, 3229.

[9] S. Kim, J. Yoon, H. D. Kim, S. J. Choi, *ACS Appl. Mater. Interfaces* **2015**, *7*, 25479.

[10] S. Choi, S. H. Tan, Z. Li, Y. Kim, C. Choi, P. Y. Chen, H. Yeon, S. Yu, J. Kim, *Nat. Mater.* **2018**, *17*, 335.

[11] G. Indiveri, S. Liu, *P. IEEE* **2015**, *103*, 1379.

[12] L. F. Abbott, W. G. Regehr, *Nature* **2004**, *431*, 796.

[13] D. Kuzum, S. Yu, H. S. P. Wong, *Nanotechnology* **2013**, *24*, 382001.

[14] W. Sun, B. Gao, M. Chi, Q. Xia, J. J. Yang, H. Qian, H. Wu, *Nat. Commun.* **2019**, *10*, 3453.

[15] M. Prezioso, F. M. Bayat, B. D. Hoskins, G. C. Adam, K. K. Likharev, D. B. Strukov, *Nature* **2015**, *521*, 61.

[16] L. F. Abbott, S. B. Nelson, *Nat. Neurosci.* **2000**, *3*, 1178.

[17] C. Mead, *P. IEEE* **1990**, *78*, 1629.

[18] H. Zhao, Z. Dong, H. Tian, D. DiMarzi, M.-G. Han, L. Zhang, X. Yan, F. Liu, L. Shen, S. J. Han, S. Cronin, W. Wu, J. Tice, J. Guo, H. Wang, *Adv. Mater.* **2017**, *29*, 1703232.

[19] Hadiyawarman, F. Budiman, D. G. O. Hernowo, R. R. Pandey, H. Tanaka, *Jpn. J. Appl. Phys.* **2018**, *57*, 03EA06.

[20] G. Rachmuth, Z. S. Harel, F. B. Mark, C. S. Poon, *Proc. Natl. Acad. Sci.* **2011**, *108*, E1266.

[21] C. Diorio, P. Hasler, A. Minch, C. A. Mead, *IEEE Trans. Electron. Devices* **1996**, *43*, 1972.

[22] Z. Wang, S. Joshi, S. Savel'ev, W. Song, R. Midya, Y. Li, M. Rao, P. Yan, S. Asapu, Y. Zhuo, H. Jiang, P. Lin, C. Li, J. H. Yoon, N. K. Upadhyay, J. Zhang, M. Hu, J. P. Strachan, M. Barnell, Q. Wu, H. Wu, R. S. Williams, Q. Xia, J. J. Yang, *Nat. Electron.* **2018**, *1*, 137.

[23] H. Tian, Q. Guo, Y. Xie, H. Zhao, C. Li, J. J. Cha, F. Xia, H. Wang, *Adv. Mater.* **2016**, *28*, 4991.

[24] T. H. Lee, D. Loke, K. J. Huang, W. J. Wang, S. R. Elliott, *Adv. Mater.* **2014**, *26*, 7493.

[25] J. Li, C. Ge, J. Du, C. Wang, G. Yang, K. Jin, *Adv. Mater.* **2020**, *32*, 1905764.

[26] S. Qin, F. Wang, Y. Liu, Q. Wan, X. Wang, Y. Xu, Y. Shi, X. Wang, R. Zhang, *2D Mater.* **2017**, *4*, 035022.

[27] M. Lee, W. Lee, S. Choi, J. W. Jo, J. Kim, S. K. Park, Y. H. Kim, *Adv. Mater.* **2017**, *29*, 1700951.

[28] S. Dai, Y. Zhao, Y. Wang, J. Zhang, L. Fang, S. Jin, Y. Shao, J. Huang, *Adv. Funct. Mater.* **2019**, *29*, 1903700.

[29] Y. Shen, N. C. Harris, S. Skirlo, M. Prabhu, T. B. Jones, M. Hochberg, X. Sun, S. Zhao, H. Larochelle, D. Englund, M. Soljačić, *Nat. Photonics* **2017**, *11*, 441.

[30] Y. Wang, L. Yin, W. Huang, Y. Li, S. Huang, Y. Zhu, D. Yang, X. Pi, *Adv. Intell. Syst.* **2021**, *3*, 2000099.

[31] Z. Cheng, C. Ríos, W. H. P. Pernice, C. D. Wright, H. Bhaskaran, *Sci. Adv.* **2017**, *3*, e1700160.

[32] G. Wang, R. Wang, W. Kong, J. Zhang, *Cogn. Neurodyn.* **2018**, *12*, 615.

[33] F. Zhou, Z. Zhou, J. Chen, T. H. Choy, J. Wang, N. Zhang, Z. Lin, S. Yu, J. Kang, H. S. P. Wong, Y. Chai, *Nat. Nanotechnol.* **2019**, *14*, 776.

[34] Y. Wang, J. Yang, W. Ye, D. She, J. Chen, Z. Lv, V. A. L. Roy, H. Li, K. Zhou, Q. Yang, Y. Zhou, S.-T. Han, *Adv. Electron. Mater.* **2020**, *6*, 1900765.

[35] J. Li, P. Dwivedi, K. S. Kumar, T. Roy, K. E. Crawford, J. Thomas, *Adv. Electron. Mater.* **2021**, *7*, 2000535.

[36] K. Liang, R. Wang, B. Huo, H. Ren, D. Li, Y. Wang, Y. Tang, Y. Chen, C. Song, F. Li, B.

Ji, H. Wang, B. Zhu, *ACS Nano* **2022**, *16*, 8651.

[37] Y. Meng, F. Li, C. Lan, X. Bu, X. Kang, R. Wei, S. Yip, D. Li, F. Wang, T. Takahashi, T. Hosomi, K. Nagashima, T. Yanagida, J. C. Ho, *Sci. Adv.* **2020**, *6*, eabc6389.

[38] G. Hu, H. An, J. Xi, J. Lu, Q. Hua, Z. Peng, *Nano Energy* **2021**, *89*, 106282.

[39] P. Xie, Y. Huang, W. Wang, Y. Meng, Z. Lai, F. Wang, S. Yip, X. Bu, W. Wang, D. Li, J. Sun, J. C. Ho, *Nano Energy* **2022**, *91*, 106654.

[40] T. Ahmed, S. Kuriakose, E. L. H. Mayes, R. Ramanathan, V. Bansal, M. Bhaskaran, S. Sriram, S. Walia, *Small* **2019**, *15*, 1900966.

[41] R. A. John, F. Liu, N. A. Chien, M. R. Kulkarni, C. Zhu, Q. Fu, A. Basu, Z. Liu, N. Mathews, *Adv. Mater.* **2018**, *30*, 1800220.

[42] N. Ilyas, J. Wang, C. Li, D. Li, H. Fu, D. Gu, X. Jiang, F. Liu, Y. Jiang, W. Li, *Adv. Func. Mater.* **2022**, *32*, 2110976.

[43] T. Luo, B. Liang, Z. Liu, X. Xie, Z. Lou, G. Shen, *Sci. Bull.* **2015**, *60*, 101.

[44] J. Michel, J. Liu, L. C. Kimerling, *Nat. Photonics* **2010**, *4*, 527.

[45] D. Zheng, H. Fang, M. Long, F. Wu, P. Wang, F. Gong, X. Wu, J. C. Ho, L. Liao, W. Hu, *ACS Nano* **2018**, *12*, 7239.

[46] D. Zheng, J. Wang, W. Hu, L. Liao, H. Fang, N. Guo, P. Wang, F. Gong, X. Wang, Z. Fan, X. Wu, X. Meng, X. Chen, W. Lu, *Nano Lett.* **2016**, *16*, 2548.

[47] C. Soci, A. Zhang, B. Xiang, S. A. Dayeh, D. P. R. Aplin, J. Park, X. Y. Bao, Y. H. Lo, D. Wang, *Nano Lett.* **2007**, *7*, 1003.

[48] Y. H. Ji, Q. Gao, A. P. Huang, M. Q. Yang, Y. Q. Liu, X. L. Geng, J. J. Zhang, R. Z. Wang, M. Wang, Z. S. Xiao, P. K. Chu, *ACS Appl. Mater. Interfaces* **2021**, *13*, 41916.

[49] G. Gou, J. Sun, C. Qian, Y. He, L. Kong, Y. Fu, G. Dai, J. Yang, Y. Gao, *J. Mater. Chem. C* **2016**, *4*, 11110.

[50] C. Shen, X. Gao, C. Chen, S. Ren, J. L. Xu, Y. D. Xia, S. D. Wang, *Nanotechnology* **2021**, *33*, 065205.

[51] D. Hao, J. Zhang, S. Dai, J. Zhang, J. Huang, *ACS Appl. Mater. Interfaces* **2020**, *12*, 39487.

[52] W. Zhao, L. Liu, M. Xu, X. Wang, T. Zhang, Y. Wang, Z. Zhang, S. Qin, Z. Liu, *Adv. Opt. Mater.* **2017**, *5*, 1700159.

[53] P. Wu, Y. Dai, T. Sun, Y. Ye, H. Meng, X. Fang, B. Yu, L. Dai, *ACS Appl. Mater. Interfaces* **2011**, *3*, 1859.

[54] H. Tan, Z. Ni, W. Peng, S. Du, X. Liu, S. Zhao, W. Li, Z. Ye, M. Xu, Y. Xu, X. Pi, D. Yang, *Nano Energy* **2018**, *52*, 422.

[55] J. Miao, W. Hu, N. Guo, Z. Lu, X. Zou, L. Liao, S. Shi, P. Chen, Z. Fan, J. C. Ho, T. X. Li, X. S. Chen, W. Lu, *ACS Nano* **2014**, *8*, 3628.

[56] K. Zhang, R. Chai, R. Shi, Z. Lou, G. Shen, *Sci. China Mater.* **2020**, *63*, 383.

[57] L. B. Luo, J. J. Chen, M. Z. Wang, H. Hu, C. Y. Wu, Q. Li, L. Wang, J. A. Huang, F. X. Liang, *Adv. Funct. Mater.* **2014**, *24*, 2794.

[58] N. Guo, W. Hu, L. Liao, S. Yip, J. C. Ho, J. Miao, Z. Zhang, J. Zou, T. Jiang, S. Wu, X. Chen, W. Lu, *Adv. Mater.* **2014**, *26*, 8203.

[59] H. Fang, W. Hu, P. Wang, N. Guo, W. Luo, D. Zheng, F. Gong, M. Luo, H. Tian, X. Zhang, C. Luo, X. Wu, P. Chen, L. Liao, A. Pan, X. Chen, W. Lu, *Nano Lett.* **2016**, *16*, 6416.

[60] D. Wu, C. Jia, F. Shi, L. Zeng, P. Lin, L. Dong, Z. Shi, Y. Tian, X. Li, J. Jie, *J. Mater. Chem. A* **2020**, *8*, 3632.

[61] L. Li, D. Wang, D. Zhang, W. Ran, Y. Yan, Z. Li, L. Wang, G. Shen, *Adv. Funct. Mater.* **2021**, *31*, 2104782.

[62] M. Jiang, Y. Zhao, L. Bian, W. Yang, J. Zhang, Y. Wu, M. Zhou, S. Lu, H. Qin, *ACS Photonics* **2021**, *8*, 3282.

[63] J. Zhang, M. Jiang, L. Bian, D. Wu, H. Qin, W. Yang, Y. Zhao, Y. Wu, M. Zhou, S. Lu, *Nanomaterials* **2021**, *11*, 2959.

[64] L. Gu, S. Poddar, Y. Lin, Z. Long, D. Zhang, Q. Zhang, L. Shu, X. Qiu, M. Kam, A. Javey, Z. Fan, *Nature* **2020**, *581*, 278.

[65] R. S. Wagner, W. C. Ellis, *Appl. Phys. Lett.* **1964**, *4*, 89.

[66] H. J. Joyce, Q. Gao, H. H. Tan, C. Jagadish, Y. Kim, J. Zou, L. M. Smith, H. E. Jackson, J. M. Y. Rice, P. J. Parkinson, *Prog. Quant. Electron.* **2011**, *35*, 23.

[67] M. A. Verheijen, G. Immink, T. Smet, M. T. Borgström, E. P. Bakkers, *J. Am. Chem. Soc.* **2006**, *128*, 1353.

[68] J. C. Harmand, M. Tchernycheva, G. Patriarche, L. Travers, F. Glas, G. Cirlin, *J. Cryst. Growth* **2007**, *301*, 853.

[69] D. Wang, X. Chen, X. Fang, J. Tang, F. Lin, X. Wang, G. Liu, L. Liao, J. C. Ho, Z. Wei, *Nanoscale* **2021**, *13*, 1086.

[70] B. Zhang, D. Fang, X. Fang, H. Zhao, D. Wang, J. Li, X. Wang, D. Wang, *Rare Metals* **2022**, *41*, 982.

[71] X. Chen, N. Xia, Z. Yang, F. Gong, Z. Wei, D. Wang, J. Tang, X. Fang, D. Fang, L. Liao, *Nanotechnology* **2018**, *29*, 095201.

[72] L. B. Luo, H. Hu, X. H. Wang, R. Lu, Y. F. Zou, Y. Q. Yu, F. X. Liang, *J. Mater. Chem.*

C **2015**, *3*, 4723.

[73] H. Ali, Y. Zhang, J. Tang, K. Peng, S. Sun, Y. Sun, F. Song, A. Falak, S. Wu, C. Qian, M. Wang, Z. Zuo, K. J. Jin, A. M. Sanchez, H. Liu, X. Xu, *Small* **2018**, *14*, 1704429.

[74] X. Dai, S. Zhang, Z. Wang, G. Adamo, H. Liu, Y. Huang, C. Couteau, C. Soci, *Nano Lett.* **2014**, *14*, 2688.

[75] Y. Ni, S. Zhang, L. Sun, L. Liu, H. Wei, Z. Xu, W. Xu, W. Xu, *Appl. Mater. Today* **2021**, *25*, 101223.

[76] X. Chen, D. Wang, T. Wang, Z. Yang, X. Zou, P. Wang, W. Luo, Q. Li, L. Liao, W. Hu, Z. Wei, *ACS Appl. Mater. Interfaces* **2019**, *11*, 33188.

[77] X. Zhu, F. Lin, X. Chen, Z. Zhang, X. Chen, D. Wang, J. Tang, X. Fang, D. Fang, L. Liao, Z. Wei, *Nanotechnology* **2020**, *31*, 444001.

[78] X. Zhu, F. Lin, Z. Zhang, X. Chen, H. Huang, D. Wang, J. Tang, X. Fang, D. Fang, J. C. Ho, L. Liao, Z. Wei, *Nano Lett.* **2020**, *20*, 2654.

[79] W. Huang, X. Xia, C. Zhu, P. Steichen, W. Quan, W. Mao, J. Yang, L. Chu, X. Li, *Nano-Micro Lett.* **2021**, *13*, 85.

[80] B. Chih, H. Engelman, P. Scheiffele, *Science* **2005**, *307*, 1324.

[81] J. Kakalios, R. A. Street, W. B. Jackson, *Phys. Rev. Lett.* **1987**, *59*, 1037.

[82] L. Q. Zhu, C. J. Wan, L. Q. Guo, Y. Shi, Q. Wan, *Nat. Commun.* **2014**, *5*, 3158.

[83] H. K. Li, T. P. Chen, P. Liu, S. G. Hu, Y. Liu, Q. Zhang, P. S. Lee, *J. Appl. Phys.* **2016**, *119*, 244505.

[84] E. Li, W. Lin, Y. Yan, H. Yang, X. Wang, Q. Chen, D. Lv, G. Chen, H. Chen, T. Guo, *ACS Appl. Mater. Interfaces* **2019**, *11*, 46008.

[85] R. S. Zucker, *Annu. Rev. Neurosci.* **1989**, *12*, 13.

[86] G. Ding, B. Yang, R. S. Chen, W. A. Mo, K. Zhou, Y. Liu, G. Shang, Y. Zhai, S.-T. Han, Y. Zhou, *Small* **2021**, *17*, 2103175.

[87] B. Mu, L. Guo, J. Liao, P. Xie, G. Ding, Z. Lv, Y. Zhou, S.-T. Han, Y. Yan, *Small* **2021**, *17*, 2103837.

[88] R. S. Zucker, W. G. Regehr, *Annu. Rev. Physiol.* **2002**, *64*, 355.

[89] Y. H. Liu, L. Q. Zhu, P. Feng, Y. Shi, Q. Wan, *Adv. Mater.* **2015**, *27*, 5599.

[90] M. Lee, S. Nam, B. Cho, O. Kwon, H. U. Lee, M. G. Hahm, U. J. Kim, H. Son, *Nano Lett.* **2021**, *21*, 7879.

[91] K. C. Kwon, Y. Zhang, L. Wang, W. Yu, X. Wang, I. H. Park, H. S. Choi, T. Ma, Z. Zhu, B. Tian, C. Su, K. P. Loh, *ACS Nano* **2020**, *14*, 7628.

[92] M. K. Kim, J. S. Lee, *Nano Lett.* **2019**, *19*, 2044.

[93] H. K. He, R. Yang, W. Zhou, H. M. Huang, J. Xiong, L. Gan, T. Y. Zhai, X. Guo, *Small* **2018**, *14*, 1800079.

[94] H. Shouval, S. Wang, G. Wittenberg, *Front. Comput. Neurosci.* **2010**, *4*, 19.

[95] R. C. Froemke, Y. Dan, *Nature* **2002**, *416*, 433.

[96] R. K. Mishra, S. Kim, S. J. Guzman, P. Jonas, *Nat. Commun.* **2016**, *7*, 11552.

[97] J. Wang, Y. Chen, L. A. Kong, Y. Fu, Y. Gao, J. Sun, *Appl. Phys. Lett.* **2018**, *113*, 151101.

[98] Y. Li, Y. Zhong, L. Xu, J. Zhang, X. Xu, H. Sun, X. Miao, *Sci. Rep.* **2013**, *3*, 1619.

[99] C. Clopath, W. Gerstner, *Front. Synaptic Neuro.* **2010**, *2*, 25.

[100] B. Berninger, G. Q. Bi, *BioEssays* **2002**, *24*, 212.

[101] S. Gao, G. Liu, H. Yang, C. Hu, Q. Chen, G. Gong, W. Xue, X. Yi, J. Shang, R. W. Li, *ACS Nano* **2019**, *13*, 2634.

[102] X. Li, B. Yu, B. Wang, R. Bi, H. Li, K. Tu, G. Chen, Z. Li, R. Huang, M. Li, *Small* **2021**, *17*, 2101434.

[103] X. Wu, S. Lan, D. Hu, Q. Chen, E. Li, Y. Yan, H. Chen, T. Guo, *J. Mater. Chem. C* **2019**, *7*, 9229.

[104] J. Zhang, T. Sun, S. Zeng, D. Hao, B. Yang, S. Dai, D. Liu, L. Xiong, C. Zhao, J. Huang, *Nano Energy* **2022**, *95*, 106987.

[105] S. Seo, S. H. Jo, S. Kim, J. Shim, S. Oh, J. H. Kim, K. Heo, J. W. Choi, C. Choi, S. Oh, D. Kuzum, H. S. P. Wong, J. H. Park, *Nat. Commun.* **2018**, *9*, 5106.

[106] M. Kumar, J. Lim, S. Kim, H. Seo, *ACS Nano* **2020**, *14*, 14108.

[107] A. Wasfi, F. Awwad, J. G. Gelovani, N. Qamhieh, A. I. Ayesh, *Nanomaterials* **2022**, *12*, 2638.

[108] J. Kim, S. K. Lee, J. H. Lee, H. Y. Kim, N. H. Kim, C. H. Lee, C. S. Lee, H. G. Kim, *Adv. Funct. Mater.* **2022**, *9*, 2102046.

[109] Q. Liu, L. Yin, C. Zhao, Z. Wu, J. Wang, X. Yu, Z. Wang, W. Wei, Y. Liu, I. Z. Mitrovic, L. Yang, E. G. Lim, C. Z. Zhao, *Nano Energy* **2022**, *97*, 107171.

[110] B. Pal, K. J. Sarkar, S. Das, P. Banerji, *J. Alloys Compd.* **2021**, *885*, 160943.

[111] Q. Liu, Y. Q. Yang, X. Wang, W. Song, X. Luo, J. Guo, J. Shi, C. Cheng, D. Li, L. He, K. Li, F. Gao, S. Li, *J. Alloys Compd.* **2021**, *864*, 158710.

[112] L. Li, Y. Zhang, R. Wang, J. Sun, Y. Si, H. Wang, C. Pan, Y. Dai, *Nano Energy* **2019**, *65*, 104046.

[113] W. Ren, Q. Tan, Q. Wang, Y. Liu, *Chem. Eng. J.* **2021**, *406*, 126779.

[114] S. Abbas, D. K. Ban, J. Kim, *Sens. Actuators. A* **2019**, *293*, 215.

[115] Z. Li, H. Li, K. Jiang, D. Ding, J. Li, C. Ma, S. Jiang, Y. Wang, T. D. Anthopoulos, Y. Shi, *ACS Appl. Mater. Interfaces* **2019**, *11*, 40204.

[116] X. Chen, B. Jiang, D. Wang, G. Li, H. Wang, H. Wang, F. Wang, P. Wang, L. Liao, Z. Wei, *Appl. Phys. Lett.* **2021**, *118*, 041102.

[117] S. S. Kizhaev, S. S. Molchanov, N. V. Zotova, E. A. Grebenshchikova, Y. P. Yakovlev, E. Hulicius, T. Šimeček, K. Melichar, J. Pangrác, *Tech. Phys. Lett.* **2001**, *27*, 964.

[118] K. K. Manga, J. Wang, M. Lin, J. Zhang, M. Nesladek, V. Nalla, W. Ji, K. P. Loh, *Adv. Mater.* **2012**, *24*, 1697.

[119] H. Algadi, C. Mahata, J. Woo, M. Lee, M. Kim, T. Lee, *Electronics* **2019**, *8*, 678.

[120] A. L. Rosa, J. Neugebauer, *Phys. Rev. B* **2006**, *73*, 205346.

[121] P. Schröer, P. Krüger, J. Pollmann, *Phys. Rev. B* **1993**, *47*, 6971.

[122] X. D. Liu, T. Xing, *Solid State Commun.* **2014**, *187*, 72.

[123] M. Ezzeldien, S. A. Qaisi, Z. A. Alrowaili, M. Alzaid, E. Maskar, A. E. Smairi, T. V. Vu, D. P. Rai, *Sci. Rep.* **2021**, *11*, 20622.

[124] C. S. Wang, B. M. Klein, *Phys. Rev. B* **1981**, *24*, 3393.

[125] Q. Cai, H. You, H. Guo, J. Wang, B. Liu, Z. Xie, D. Chen, H. Lu, Y. Zheng, R. Zhang, *Light: Sci. Appl.* **2021**, *10*, 94.

[126] Y. Chen, W. Qiu, X. Wang, W. Liu, J. Wang, G. Dai, Y. Yuan, Y. Gao, J. Sun, *Nano Energy* **2019**, *62*, 393.

[127] O. Kurniawan, L. E. Ping, presented at 12th Int. Symp. Integr. Circuits, Singapore, Dec. **2009**.

[128] M. Kumar, S. Abbas, J. Kim, *ACS Appl. Mater. Interfaces* **2018**, *10*, 34370.

[129] M. Kumar, J. Kim, C. P. Wong, *Nano Energy* **2019**, *63*, 103843.

[130] C. J. O'Kelly, J. A. Fairfield, D. McCloskey, H. G. Manning, J. F. Donegan, J. J. Boland, *Adv. Electron. Mater.* **2016**, *2*, 1500458.

[131] C. Zha, X. Yan, X. Yuan, Y. Zhang, X. Zhang, *Opt. Quantum Electron.* **2021**, *53*, 587.

[132] B. Li, W. Wei, X. Yan, X. Zhang, P. Liu, Y. Luo, J. Zheng, Q. Lu, Q. Lin, X. Ren, *Nanotechnology* **2018**, *29*, 464004.

[133] J. Jiang, W. Hu, D. Xie, J. Yang, J. He, Y. Gao, Q. Wan, *Nanoscale* **2019**, *11*, 1360.

[134] Z. D. Luo, X. Xia, M. M. Yang, N. R. Wilson, A. Gruverman, M. Alexe, *ACS Nano* **2020**, *14*, 746.

[135] T. Ahmed, M. Tahir, M. X. Low, Y. Ren, S. A. Tawfik, E. L. H. Mayes, S. Kuriakose, S. Nawaz, M. J. S. Spencer, H. Chen, M. Bhaskaran, S. Sriram, S. Walia, *Adv. Mater.* **2021**, *33*, 2004207.

[136] M. Xu, T. Xu, A. Yu, H. Wang, H. Wang, M. Zubair, M. Luo, C. Shan, X. Guo, F. Wang, W. Hu, Y. Zhu, *Adv. Opt. Mater.* **2021**, *9*, 2100937.

[137] Y. Sun, M. Li, Y. Ding, H. Wang, H. Wang, Z. Chen, D. Xie, *InfoMat* **2022**, e12317.

[138] W. Huang, P. Hang, Y. Wang, K. Wang, S. Han, Z. Chen, W. Peng, Y. Zhu, M. Xu, Y. Zhang, Y. Fang, X. Yu, D. Yang, X. Pi, *Nano Energy* **2020**, *73*, 104790.

[139] Y. Wang, Z. Lv, J. Chen, Z. Wang, Y. Zhou, L. Zhou, X. Chen, S.-T. Han, *Adv. Mater.* **2018**, *30*, 1802883.

[140] B. Pradhan, S. Das, J. Li, F. Chowdhury, J. Cherusseri, D. Pandey, D. Dev, A. Krishnaprasad, E. Barrios, A. Towers, A. Gesquiere, L. Tetard, T. Roy, J. Thomas, *Sci. Adv.* **2020**, *6*, eaay5225.

[141] E. Ercan, Y. C. Lin, W. C. Yang, W. C. Chen, *Adv. Funct. Mater.* **2022**, *32*, 2107925.

[142] H. Duan, L. Liang, Z. Wu, H. Zhang, L. Huang, H. Cao, *ACS Appl. Mater. Interfaces* **2021**, *13*, 30165.

[143] D. Li, C. Li, N. Ilyas, X. Jiang, F. Liu, D. Gu, M. Xu, Y. Jiang, W. Li, *Adv. Intell. Syst.* **2020**, *2*, 2000107.

[144] R. Lin, X. Liu, G. Zhou, Z. Qian, X. Cui, P. Tian, *Adv. Opt. Mater.* **2021**, *9*, 2002211.

[145] D. Yu, F. Cao, Y. Gu, Z. Han, J. Liu, B. Huang, X. Xu, H. Zeng, *Nano Res.* **2021**, *14*, 1210.

[146] X. Sun, C. H. Kang, M. Kong, O. Alkhazragi, Y. Guo, M. Ouhssain, Y. Weng, B. H. Jones, T. K. Ng, B. S. Ooi, *J. Lightwave Technol.* **2020**, *38*, 421.

[147] H. Chen, X. Chen, J. Lu, X. Liu, J. Shi, L. Zheng, R. Liu, X. Zhou, P. Tian, *IEEE Photonics J.* **2020**, *12*, 1.

[148] Z. Lv, G. He, C. Qiu, Y. Fan, H. Wang, Z. Liu, *Opt. Express* **2021**, *29*, 16197.

[149] K. Park, M. Jung, D. Kim, J. R. Bayogan, J. H. Lee, S. J. An, J. Seo, J. Seo, J. P. Ahn, J. Park, *Nano Lett.* **2020**, *20*, 4939.

[150] Y. Yang, X. Peng, H. S. Kim, T. Kim, S. Jeon, H. K. Kang, W. Choi, J. Song, Y. J. Doh, D. Yu, *Nano Lett.* **2015**, *15*, 5875.

[151] Y. Han, M. Fu, Z. Tang, X. Zheng, X. Ji, X. Wang, W. Lin, T. Yang, Q. Chen, *ACS Appl. Mater. Interfaces* **2017**, *9*, 2867.

[152] J. A. A. Webber, C. K. Groschner, A. A. Sagade, G. Tainter, M. F. G. Zalba, R. D. Pietro, J. W. Leung, H. H. Tan, C. Jagadish, S. Hofmann, H. J. Joyce, *ACS Appl. Mater. Interfaces* **2017**, *9*, 43993.

[153] B. Li, X. Yan, X. Zhang, Y. Luo, Q. Lu, X. Ren, *Appl. Phys. Lett.* **2017**, *111*, 113102.

[154] E. Baek, T. Rim, J. Schütt, C. Baek, K. Kim, L. Baraban, G. Cuniberti, *Nano Lett.* **2017**,

17, 6727.

[155] J. W. John, V. Dhyani, Y. M. Georgiev, A. S. Gangnaik, S. Biswas, J. D. Holmes, A. K. Das, S. K. Ray, S. Das, *ACS Appl. Electron. Mater.* **2020**, *2*, 1934.

[156] X. Zhang, Z. Li, X. Yao, H. Huang, D. Wei, C. Zhou, Z. Tang, X. Yuan, P. Chen, W. Hu, J. Zou, W. Lu, L. Fu, *ACS Appl. Electron. Mater.* **2019**, *1*, 1825.

[157] Y. Guo, D. Liu, C. Miao, J. Sun, Z. Pang, P. Wang, M. Xu, N. Han, Z. X. Yang, *Nanotechnology* **2021**, *32*, 145203.

[158] X. Yao, X. Zhang, Q. Sun, D. Wei, P. Chen, J. Zou, *ACS Appl. Mater. Interfaces* **2021**, *13*, 5691.

[159] E. Zarezadeh, A. Ghorbani, *Mater. Res. Express* **2020**, *7*, 056203.

[160] V. Kumar, K. Kumar, H. C. Jeon, T. W. Kang, D. Lee, S. Kumar, *J. Phys. Chem. Solids* **2019**, *124*, 1.

[161] S. Zhao, J. Sun, Y. Yin, Y. Guo, D. Liu, C. Miao, X. Feng, Y. Wang, M. Xu, Z. X. Yang, *J. Phys. Chem. Lett.* **2021**, *12*, 3046.

[162] H. M. Huang, R. S. Chen, H. Y. Chen, T. W. Liu, C. C. Kuo, C. P. Chen, H. C. Hsu, L. C. Chen, K. H. Chen, Y. J. Yang, *Appl. Phys. Lett.* **2010**, *96*, 062104.

[163] X. Zhang, J. Jie, Z. Wang, C. Wu, L. Wang, Q. Peng, Y. Yu, P. Jiang, C. Xie, *J. Mater. Chem.* **2011**, *21*, 6736.

[164] E. Oksenberg, R. P. Biro, K. Rechav, E. Joselevich, *Adv. Mater.* **2015**, *27*, 3999.

[165] Y. Yan, W. Ran, Z. Li, L. Li, Z. Lou, G. Shen, *Nano Res.* **2021**, *14*, 3379.

[166] D. H. Sliney, *Ophthalmology* **1983**, *90*, 937.

[167] Y. Lee, Y. O. Jin, W. Xu, O. Kim, R. K. Taeho, J. Kang, Y. Kim, D. Son, B. H. T. Jeffery, J. P. Moon, Z. Bao, T. W. Lee, *Sci. Adv.* **2018**, *4*, eaat7387.

[168] R. Shapley, M. Hawken, D. L. Ringach, *Neuron* **2003**, *38*, 689.

[169] W. S. Geisler, D. G. Albrecht, *Visual Neurosci.* **1997**, *14*, 897.

[170] C. J. McAdams, J. H. R. Maunsell, *J. Neurosci.* **1999**, *19*, 431.

[171] S. Zhao, Z. Ni, H. Tan, Y. Wang, H. Jin, T. Nie, M. Xu, X. Pi, D. Yang, *Nano Energy* **2018**, *54*, 383.

[172] L. Yin, C. Han, Q. Zhang, Z. Ni, S. Zhao, K. Wang, D. Li, M. Xu, H. Wu, X. Pi, D. Yang, *Nano Energy* **2019**, *63*, 103859.

[173] Q. Zhang, T. Jin, X. Ye, D. Geng, W. Chen, W. Hu, *Adv. Funct. Mater.* **2021**, *31*, 2106151.

[174] J. Tersoff, *Nano Lett.* **2015**, *15*, 6609.

[175] J. Yao, H. Yan, C. M. Lieber, *Nat. Nanotechnol.* **2013**, *8*, 329.

[176] K. Peng, D. Jevtics, F. Zhang, S. Sterzl, D. A. Damry, M. U. Rothmann, B. Guilhabert, M. J. Strain, H. H. Tan, L. M. Herz, L. Fu, M. D. Dawson, A. Hurtado, C. Jagadish, M. B. Johnston, *Science* **2020**, *368*, 510.

[177] C. M. Yang, T. C. Chen, D. Verma, L. J. Li, B. Liu, W. H. Chang, C. S. Lai, *Adv. Funct. Mater.* **2020**, *30*, 2001598.

[178] X. Li, Z. Xu, C. Zhao, S. W. Zhang, J. Li, F. Kang, Q. Song, G. Wei, *Adv. Opt. Mater.* **2022**, 2200583.

[179] M. Takiguchi, S. Sasaki, K. Tateno, E. Chen, K. Nozaki, S. Sergent, E. Kuramochi, G. Zhang, A. Shinya, M. Notomi, *ACS Photonics* **2020**, *7*, 3467.

[180] J. Wang, Y. Long, *Sci. Bull.* **2018**, *63*, 1267.

[181] Z. Wang, X. Zhang, D. Wu, J. Guo, Z. Zhao, Z. Shi, Y. Tian, X. Huang, X. Li, *J. Mater. Chem. C* **2020**, *8*, 6877.

[182] S. Tongay, W. Fan, J. Kang, J. Park, U. Koldemir, J. Suh, D. S. Narang, K. Liu, J. Ji, J. Li, R. Sinclair, J. Wu, *Nano Lett.* **2014**, *14*, 3185.

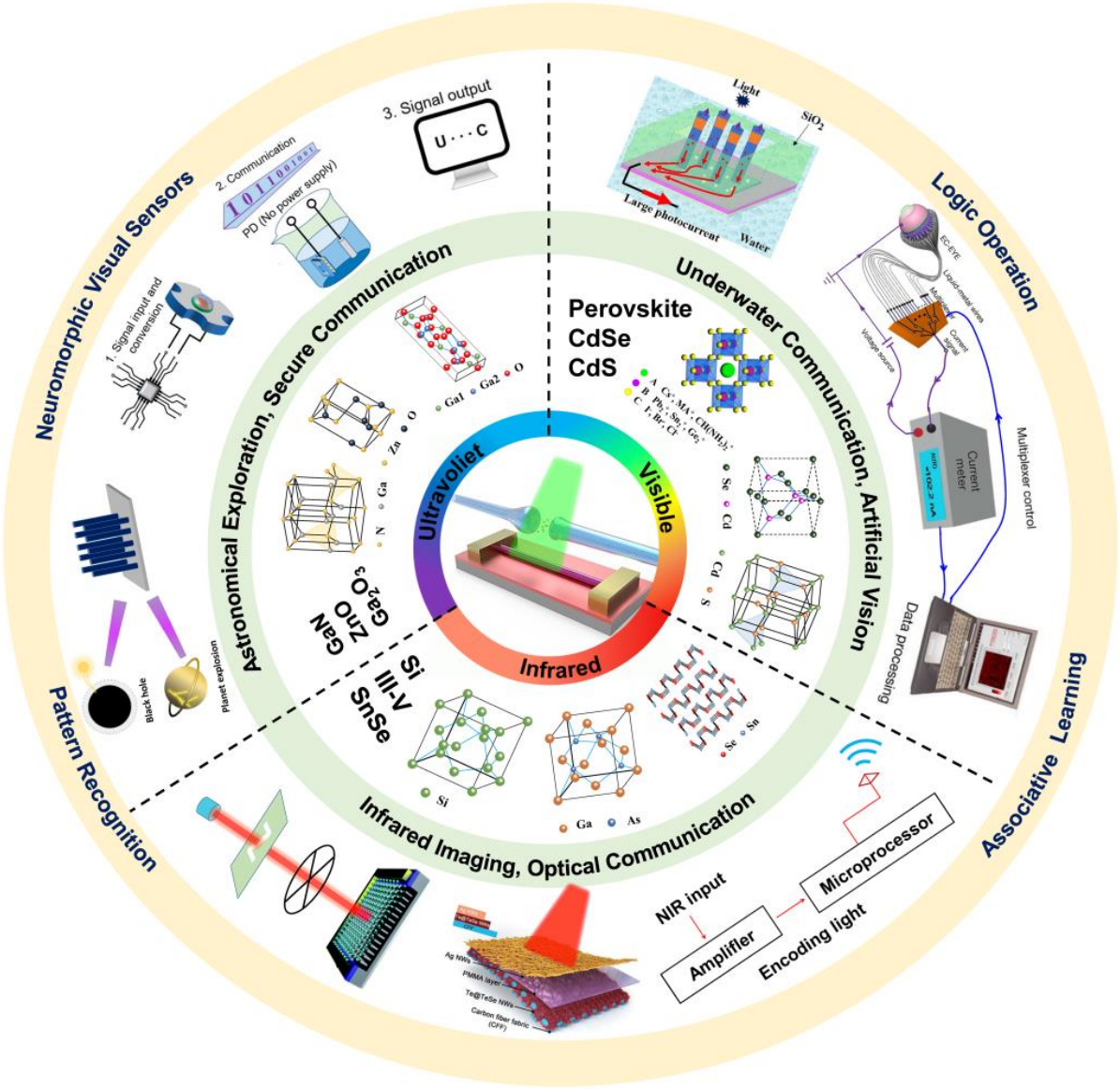

Figure 1. Overview of this review.[60-64] Reproduced with permission.[60] Copyright 2020, The Royal Society of Chemistry. Reproduced with permission.[61] Copyright 2021, Wiley-VCH GmbH. Reproduced with permission.[62] Copyright 2021, American Chemical Society. Reproduced with permission.[63] Copyright 2021, MDPI. Reproduced with permission.[64] Copyright 2020, Springer Nature.

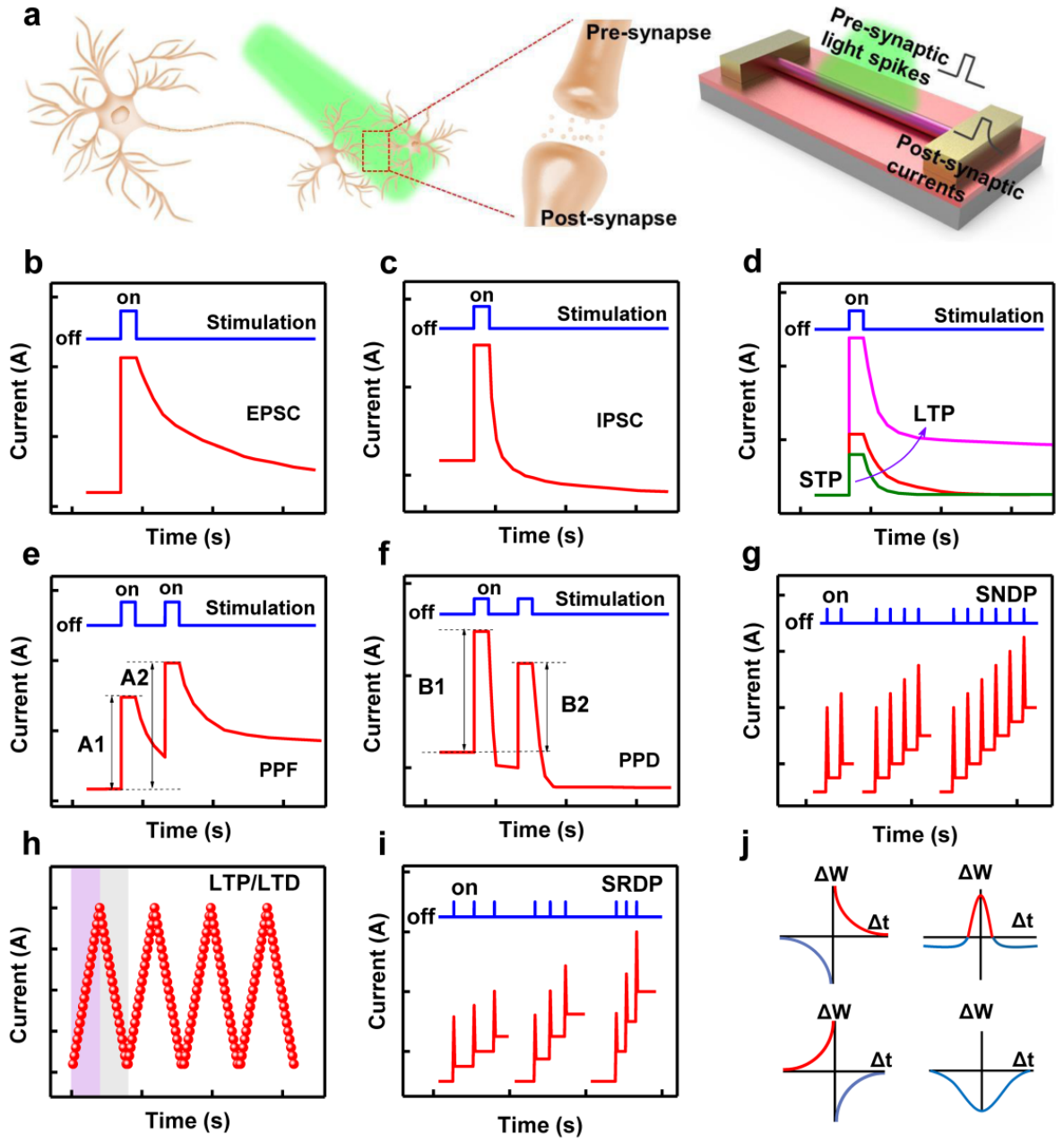

Figure 2. The basic functionalities of synaptic devices. a) The schematic diagram of biological and artificial synapse structures. b) EPSC. c) IPSC. d) Short-term plasticity, long-term plasticity, and the transition from short-term plasticity to long-term plasticity. e) PPF. f) PPD. g) SNDP. h) LTP/LTD. i) SRDP. j) STDP. Reproduced with permission.[37] Copyright 2020, American Association for the Advancement of Science. Reproduced with permission. [94] Copyright 2010, Frontiers.

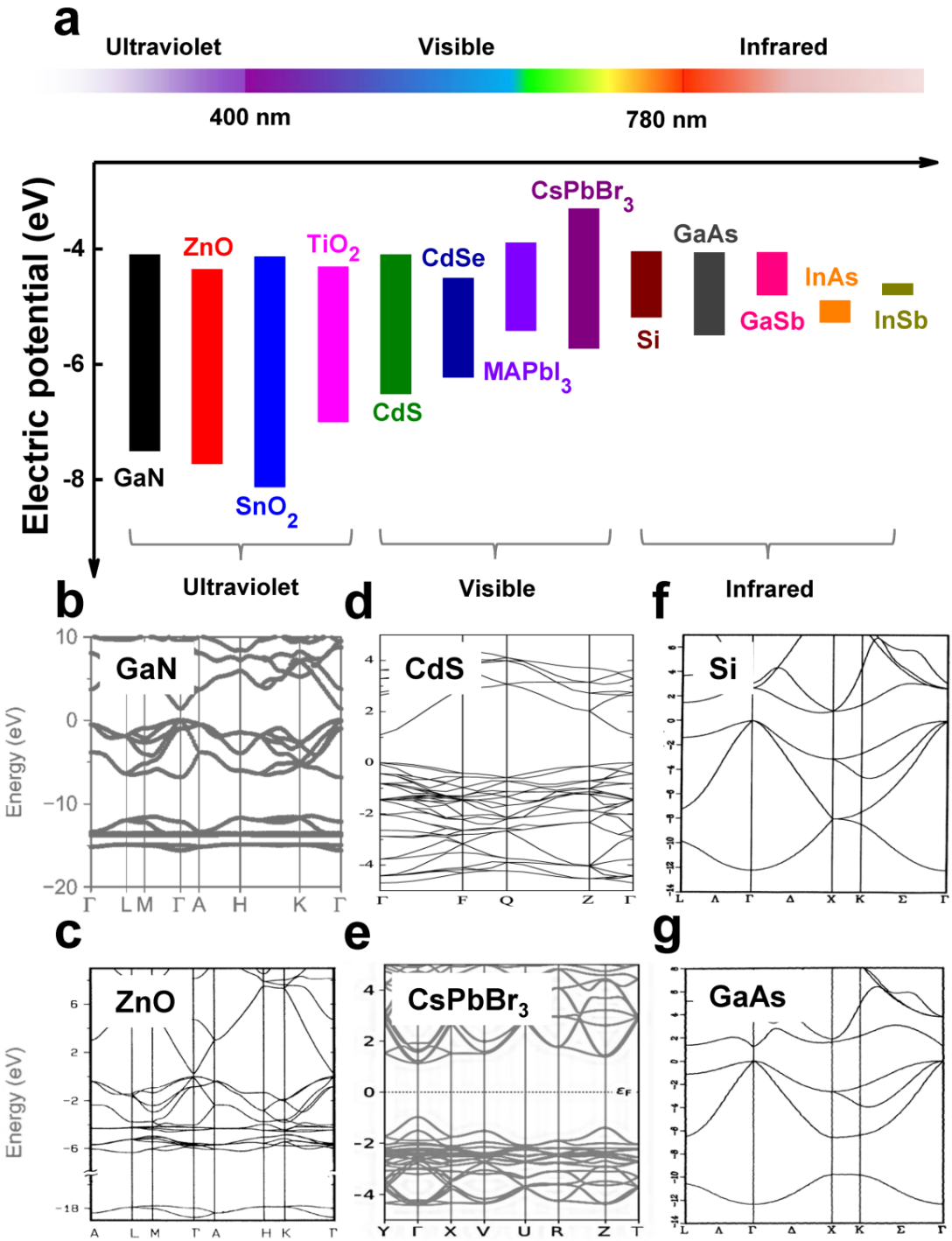

Figure 3. a) Some typical ultraviolet-visible-infrared optoelectronic materials.[110-119] Band structures of b) GaN. Reproduced with permission.[120] Copyright 2006, The American Physical Society. c) ZnO. Reproduced with permission.[121] Copyright 1993, The American Physical Society. d) CdS. Reproduced with permission.[122] Copyright 2014, Elsevier Ltd. e) $CsPbBr_3$. Reproduced with permission.[123] Copyright 2021, Springer Nature. f) Si.[124] g) GaAs. Reproduced with permission.[124] Copyright 1981, The American Physical Society.

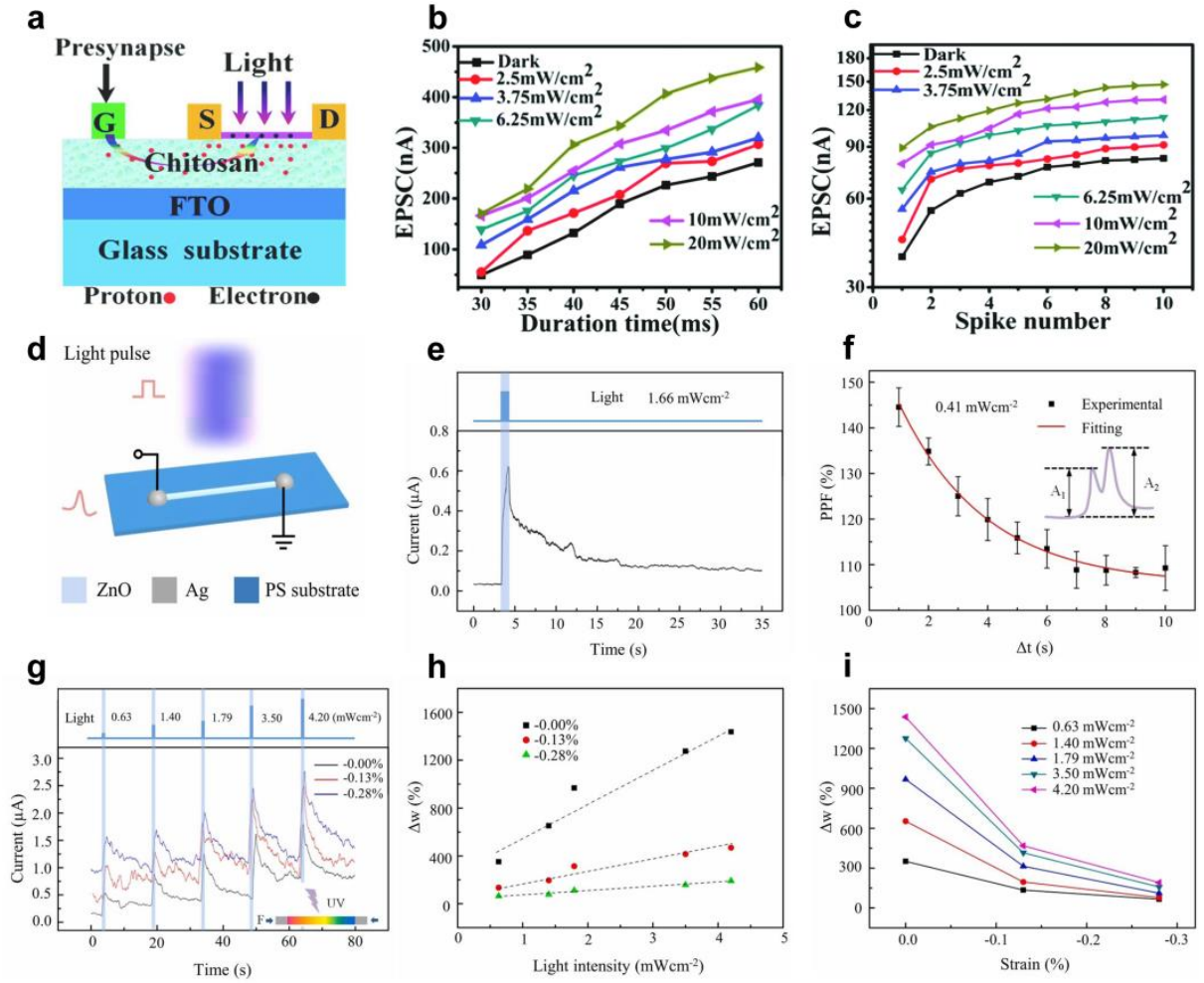

Figure 4. a) Schematic illustration of the SnO_2 NW synaptic devices. b) Dependence of EPSC and light duration time. c) Dependence of EPSC and light spike number. Reproduced with permission.[49] Copyright 2016, The Royal Society of Chemistry. d) Schematic illustration of ZnO NW photonic synapse. e) EPSC triggered by light. f) PPF index. g) Dependence of EPSC and light intensity. h) Dependence of synaptic weight change and light intensity. i) Dependence of synaptic weight change and strains. Reproduced with permission.[38] Copyright 2021, Elsevier Ltd.

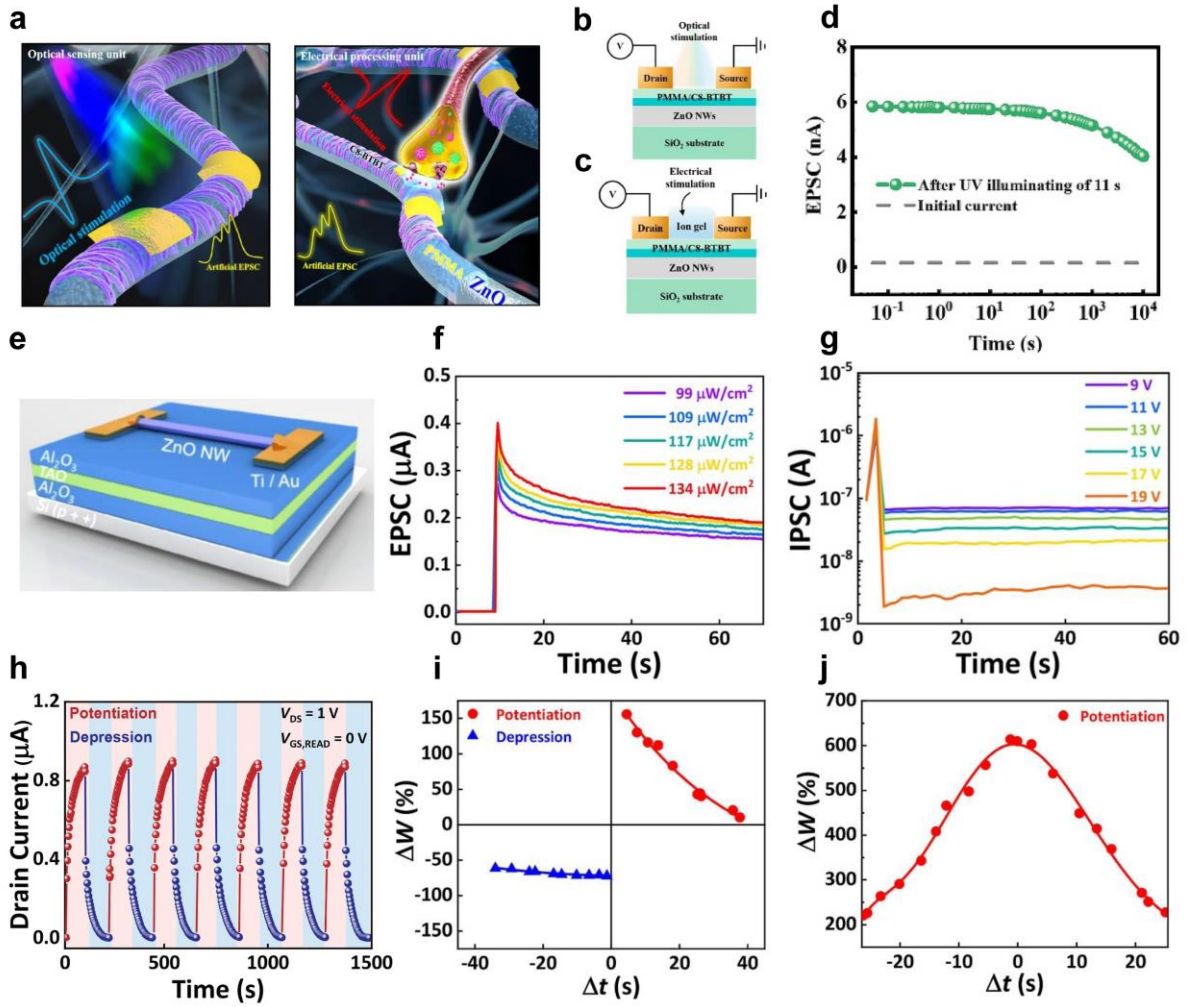

Figure 5. a) The PMMA/C8-BTBT decorated ZnO NWs based p-i-n heterojunction neuromorphic transistor with electro-optical pulse. b) A cross-sectional view of the device as an optical sensing unit. c) A cross-sectional view of device as an electrical processing unit. d) Current retention of the ZnO NWs device after UV illumination. Reproduced with permission.[75] Copyright 2021, Elsevier Ltd. e) Schematic device structure of a single ZnO NW synaptic transistor. f) EPSC varies with different UV light power density. g) PSC varies with different electrical spikes. h) Multiple cycles of LTP/LTD. i) Asymmetric STDP. j) Symmetric STDP. Reproduced with permission.[50] Copyright 2021, IOP Publishing Ltd.

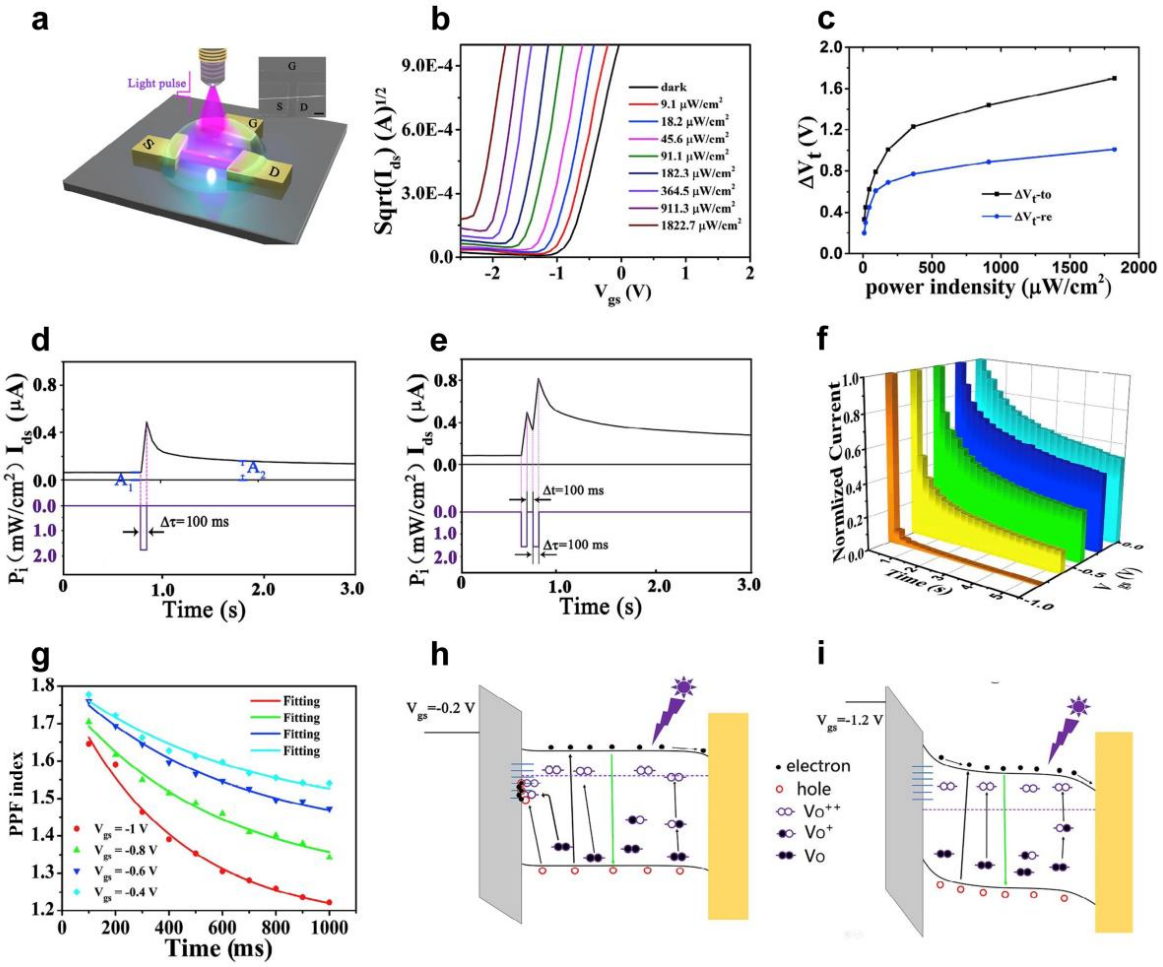

Figure 6. a) Device structure of a SnO_2 NW solar blind ultraviolet optoelectronic synaptic transistor. b) Transfer curves with different solar blind ultraviolet light intensities. c) Change in threshold voltage as a function of solar blind ultraviolet light intensity. d) EPSC. e) PPF. f) EPSC as a function of time and gate voltages. g) PPF index. h-i) Energy-band diagrams at the dielectric-semiconductor interface with different gate voltage under illumination. Reproduced with permission.[126] Copyright 2019, Elsevier Ltd.

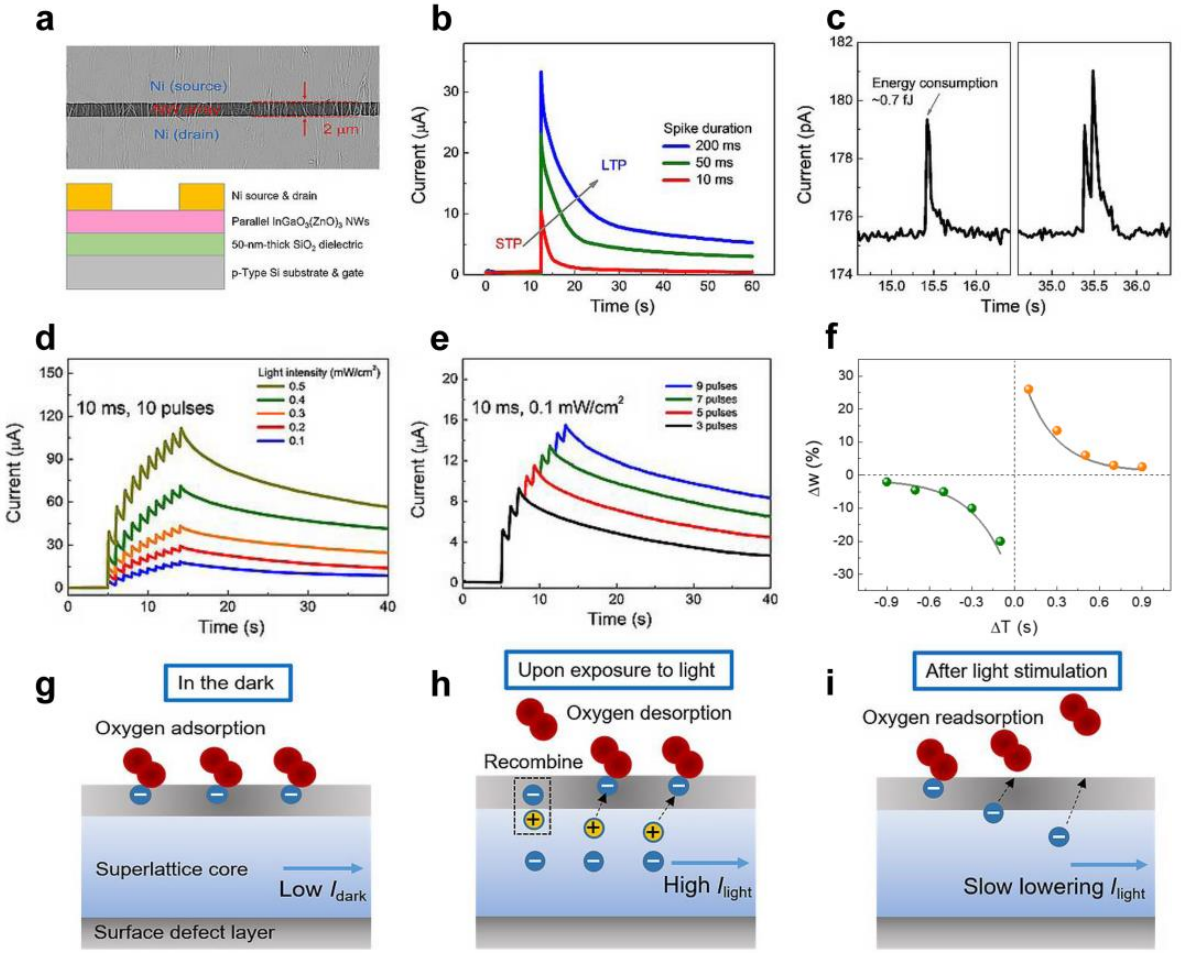

Figure 7. a) Schematic illustration and corresponding SEM image of the $InGaO_3(ZnO)_3$ superlattice NW photonic synapses. b) Transition from short-term plasticity to long-term plasticity under light spike with different spike duration time. c) EPSC and PPF. d) Light intensity-dependent plasticity of the device. e) SNDP. f) Asymmetric Hebbian learning STDP behaviors. g-i) Schematics of oxygen adsorption-induced charge trapping and subsequent optically induced charge release on $InGaO_3(ZnO)_3$ superlattice NWs. Reproduced with permission.[37] Copyright 2020, American Association for the Advancement of Science.

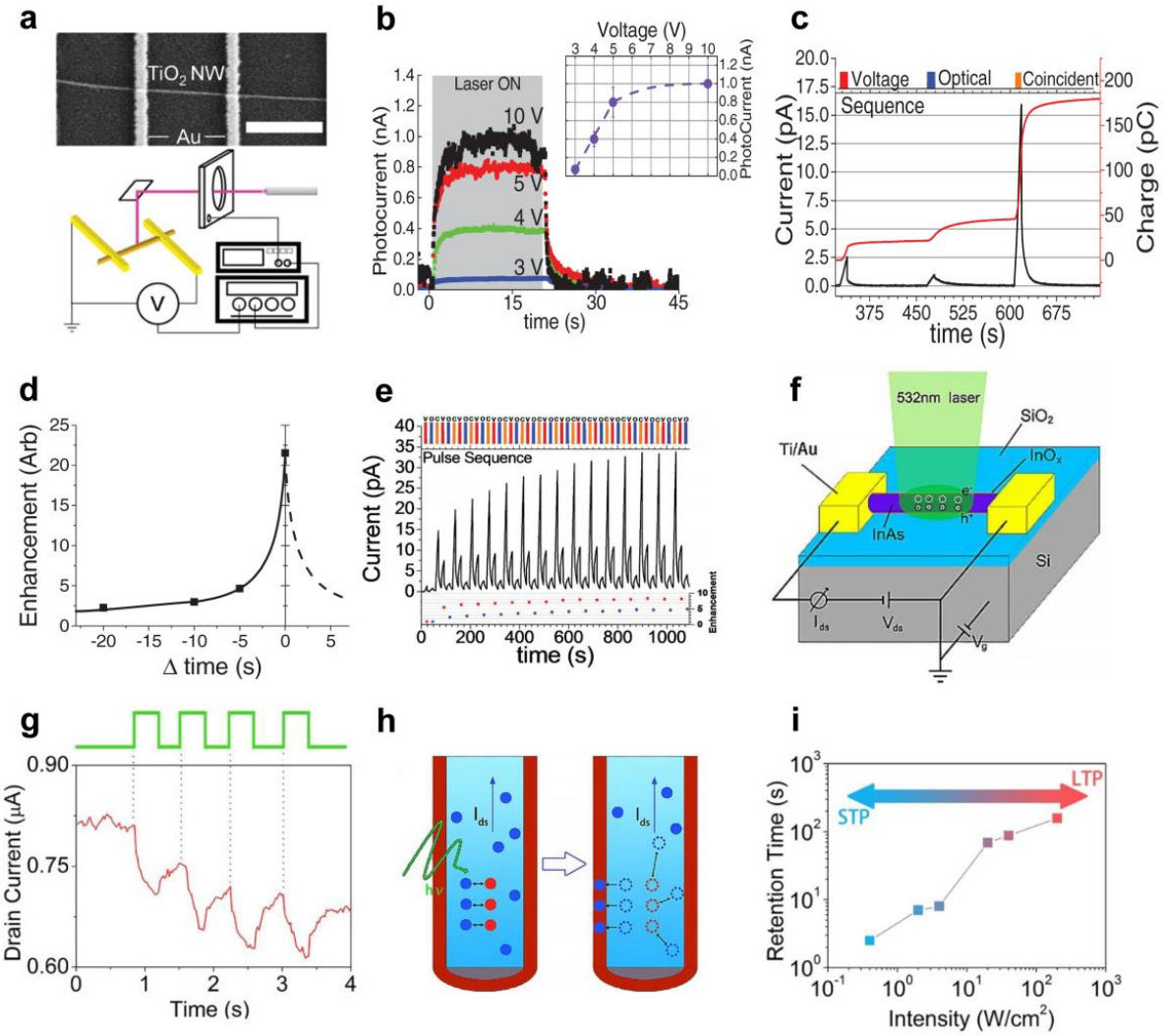

Figure 8. a) SEM image of the TiO_2 NW based visible optoelectronic synaptic device with Au contacts (scale bar: 1 μm) and the schematic of the experimental setup. b) Light-induced EPSC with different voltages. c) EPSC triggered by voltage pulse, optical pulse and a coincident pulse consisting of both voltage pulse and optical pulse. d) A pseudo-plasticity strengthening graph analogous to STDP displaying the enhancement of device conductance as the time interval between pulses decreases. e) A plot showing the device response to a series of coincident pulses that result in a growing and heightened current output, consistent with a learning phenomenon. Reproduced with permission.[130] Copyright 2016, Wiley-VCH GmbH & Co. KGaA. f) Schematic diagram of the InAs NW phototransistor. g) PSC of the device under illumination. h) The mechanism of the reduction current in the InAs NW channel. i) The retention time of the synaptic weight to the initial state under different light intensities. Reproduced with permission.[132] Copyright 2018, IOP Publishing Ltd.

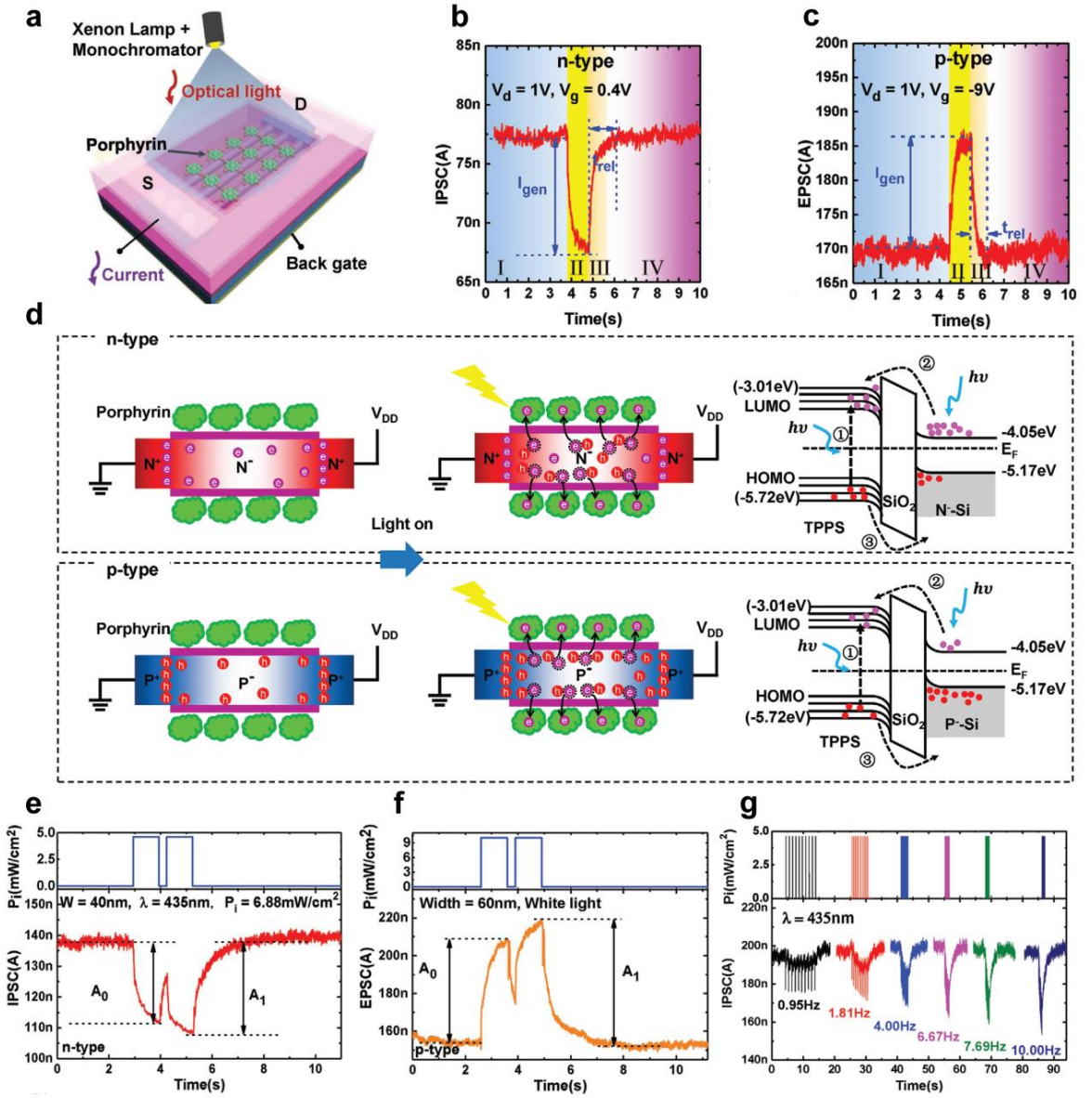

Figure 9. a) The schematic diagram of a light-stimulated porphyrin and Si NW hybrid synaptic device. b) IPSC of n-type Si NW device triggered by light. c) EPSC of p-type Si NW device triggered by light. d) Schematic diagram of the carrier distribution in n-type and p-type Si NWs with TPPS modification. (e) PPD characteristics of n-type Si NW device triggered by light. f) PPF characteristics of p-type Si NW device triggered by light. g) Dynamic filtering characteristics of the n-type Si NW device. Reproduced with permission.[102] Copyright 2021, Wiley-VCH GmbH.

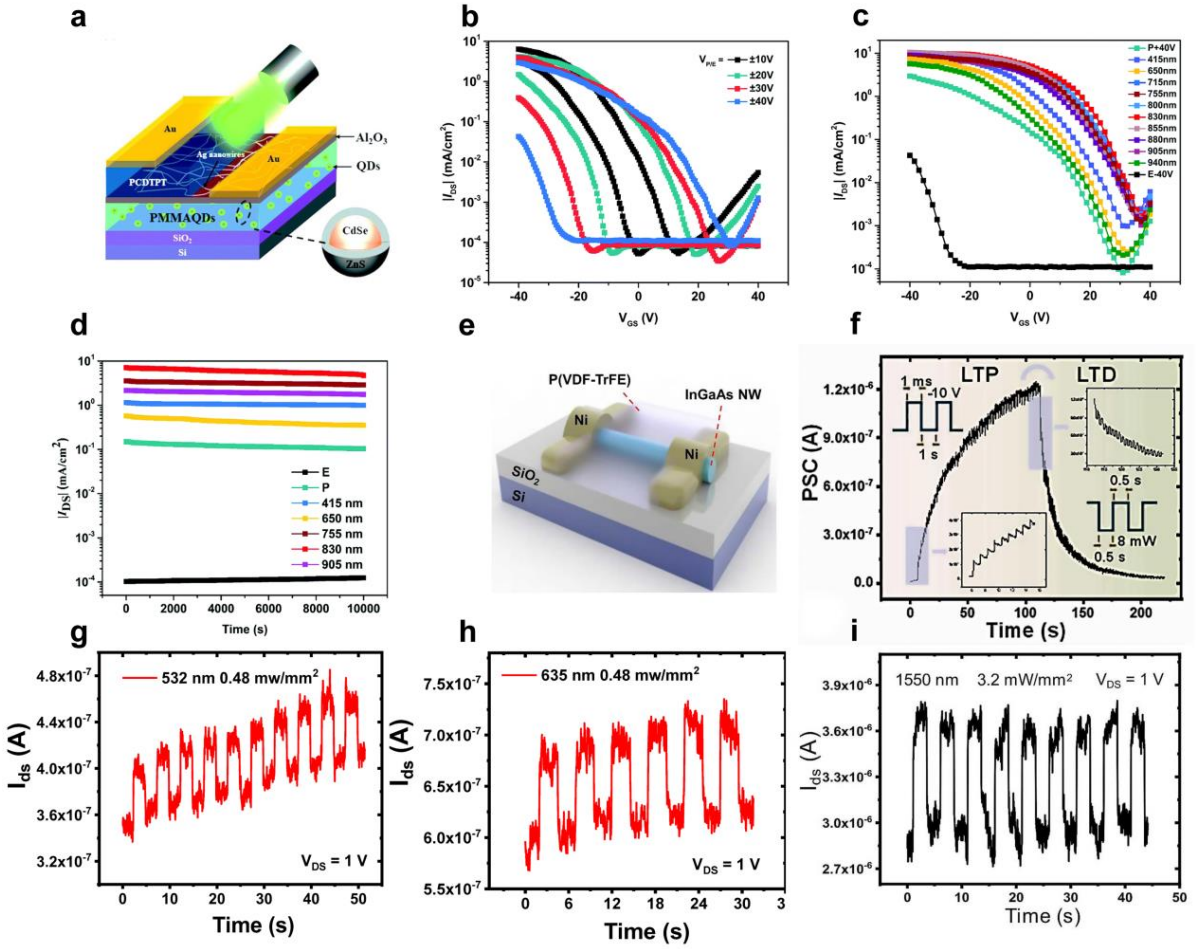

Figure 10. a) Schematic diagram of the Ag NWs/PCDTPT film based vertical organic field effect transistor. b) Transfer characteristic curves of the device as a function of the different programming gate voltages. c) Transfer characteristics curve of the device when triggered by various wavelength light illumination after programming. d) Retention characteristics of the device when triggered by various wavelength light illumination. Reproduced with permission.[103] Copyright 2019, The Royal Society of Chemistry. e) Schematic diagram of the ferroelectric P(VDF-TrFE) wrapped InGaAs NW artificial synaptic device. f) LTP/LTD characteristics realized by electric and visible light pulses. g-i) The response in the visible to infrared band of synaptic devices. Reproduced with permission.[39] Copyright 2021, Elsevier Ltd.

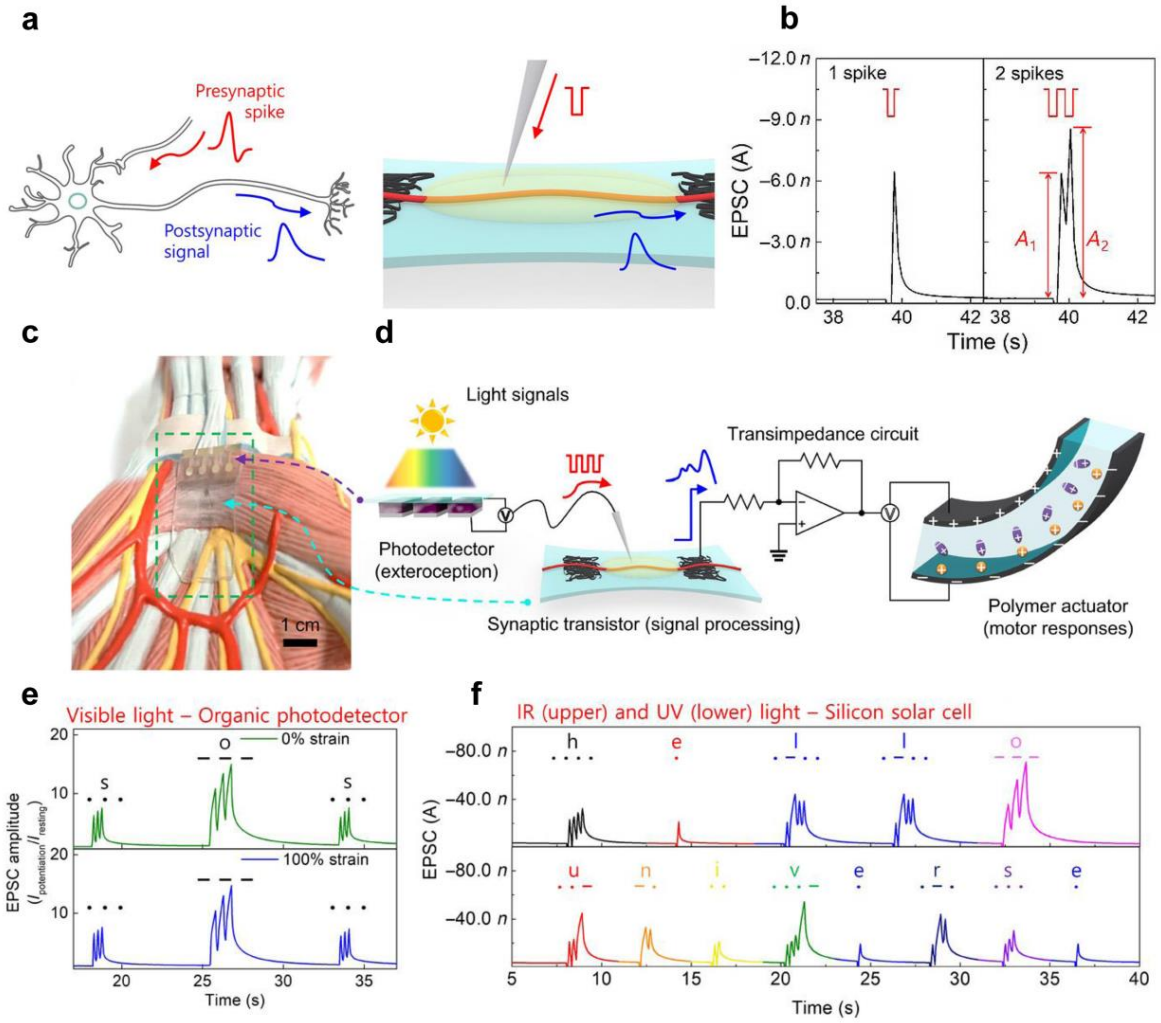

Figure 11. a) Neural signal transmission from pre-neuron to post-neuron through a biological synapse (left) and an artificial synapse (right). b) EPSCs triggered by single and double spikes. c) Photograph of organic optoelectronic synapse on an internal human structure model. d) Configuration of organic optoelectronic synapse (photodetector and artificial synapse) and neuromuscular electronic system (artificial synapse, transimpedance circuit, and artificial muscle actuator). e) Visible light-triggered EPSC amplitudes of organic NW synaptic transistor with the International Morse code of "SOS". f) Infrared and ultraviolet light-triggered EPSC amplitudes of organic NW synaptic transistor with the International Morse code of "HELLO UNIVERSE". Reproduced with permission.[167] Copyright 2018, American Association for the Advancement of Science.

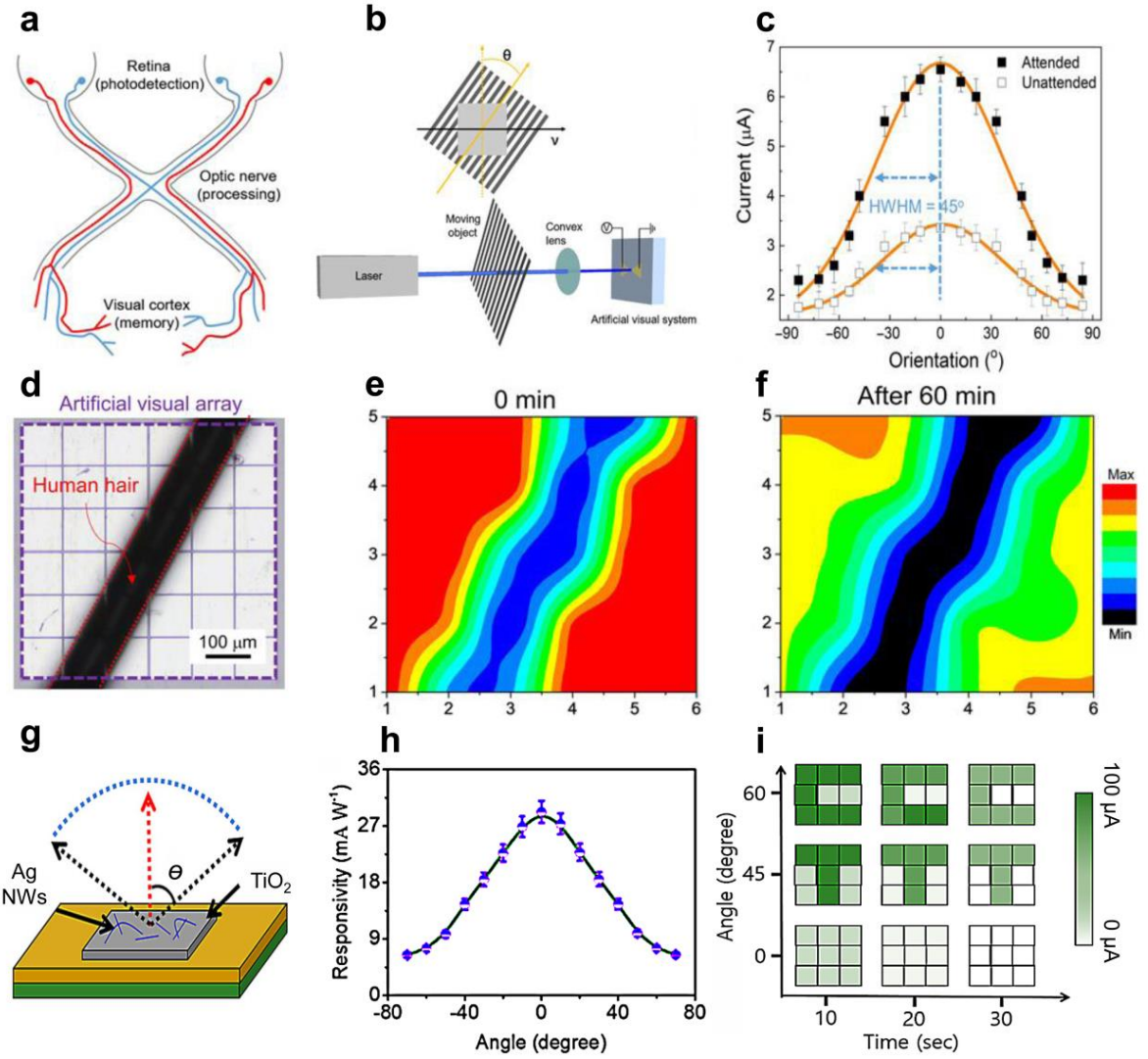

Figure 12. a) Schematic diagram of the human visual system. b) Schematic diagram of orientation dependence experiment based on $InGaO_3(ZnO)_3$ superlattice NWs photonic synapses. c) The dependence of visual response and orientation angle. d-f) Imaging processing and memorizing behaviors of the device when exposed to hair-shaped patterned light. Reproduced with permission.[37] Copyright 2020, American Association for the Advancement of Science. g) Schematic diagram of Ag NW/TiO_2 Schottky optoelectronic synaptic device. h) Light sensitivity as a function of the illumination angle. i) Optoelectronic coupling dependent memorization behavior of the device array. Reproduced with permission.[106] Copyright 2020, American Chemical Society.

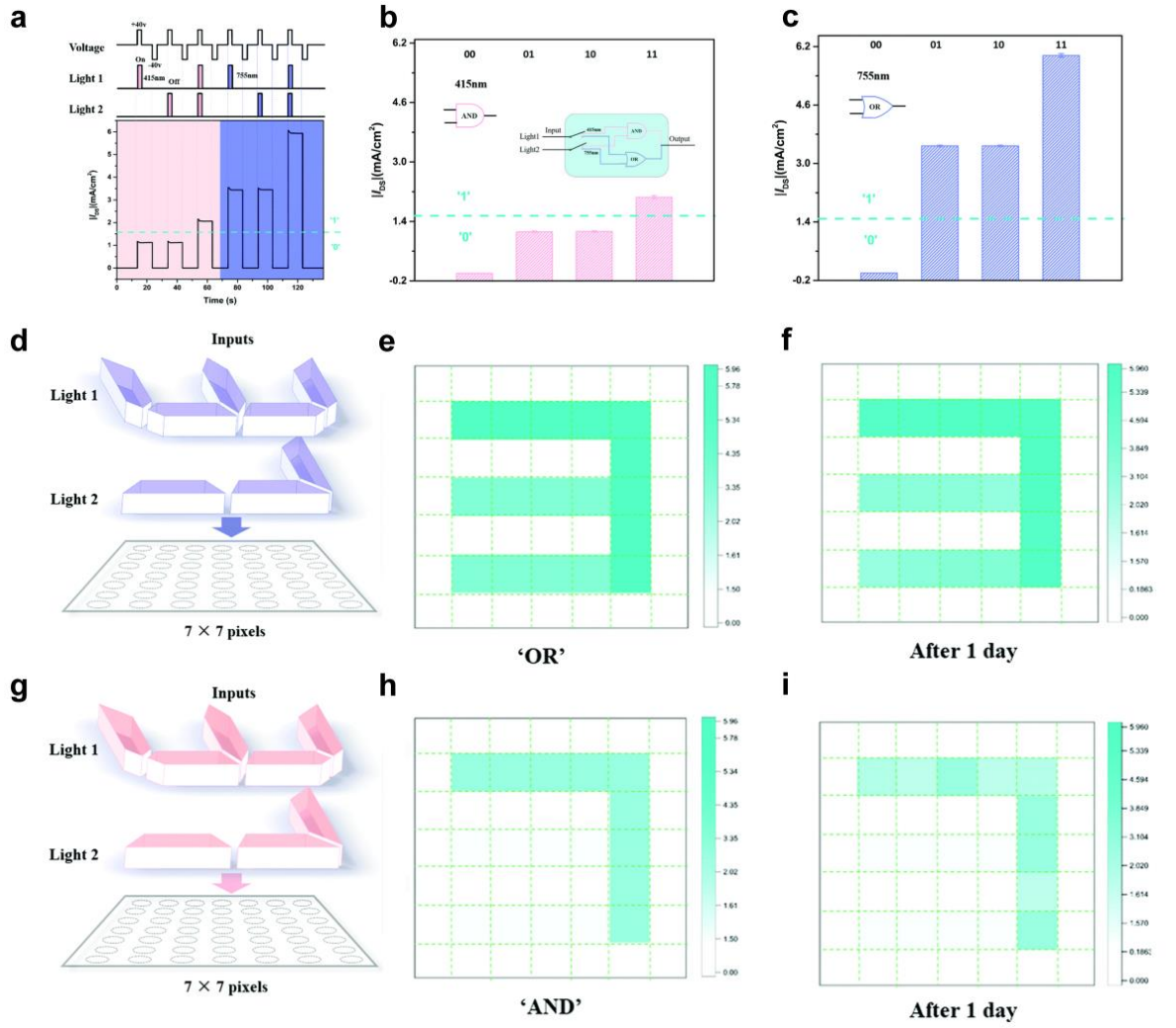

Figure 13 a) The current dependent on the operating sequence of two light signals and gate voltage. b) The input signals is 415 nm illumination and +40 V gate voltage, and the inset is the schematic diagram of the logic operation switching under different wavelengths. c) Logic gate "OR" realized by 755 nm illumination and +40 V gate voltage. d-f) Image processing and memorizing behaviors of the Ag NWs/PCDTPT film floating-gate transistor array under logic gate "OR". g-i) Image processing and memorizing behaviors of the Ag NWs/PCDTPT film floating-gate transistor array under logic gate "AND". Reproduced with permission.[103] Copyright 2019, The Royal Society of Chemistry.

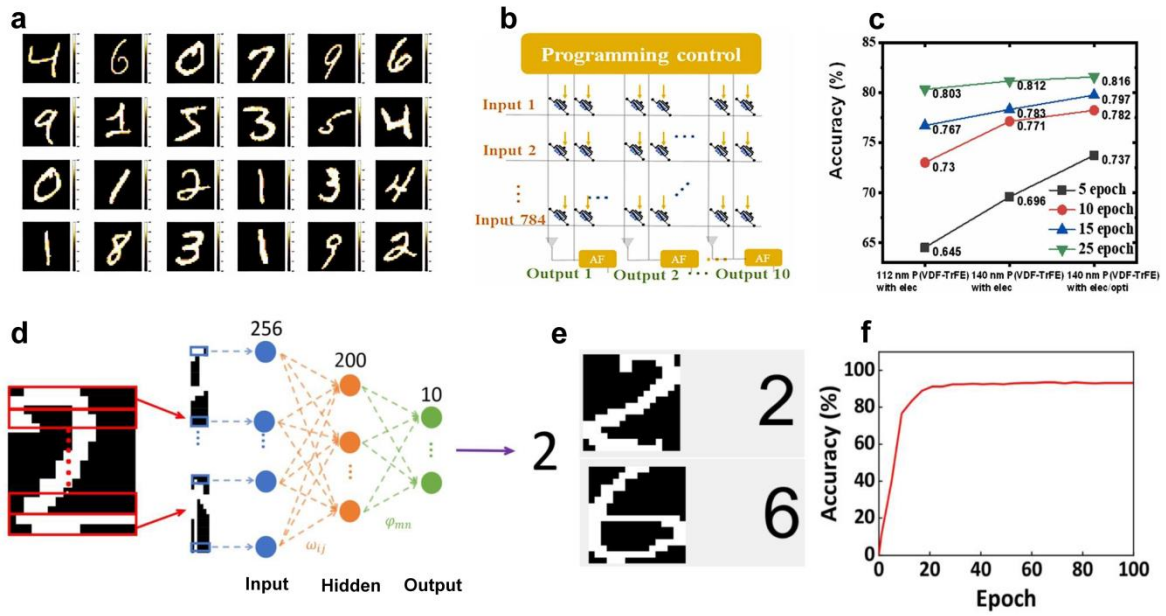

Figure 14. a) Supervised learning based on the MNIST database simulated by P(VDF-TrFE) wrapped InGaAs NW optoelectronic synaptic transistors. b) Schematic diagram of the single layer perceptron ANN. c) Training results. Reproduced with permission.[39] Copyright 2021, Elsevier Ltd. d) Schematic illustration of ANN simulation based on ZnO NW optoelectronic synaptic transistors. e) Recognition results of Numbers "2" and "6". f) Recognition accuracy versus training epoch in the simulation. Reproduced with permission.[50] Copyright 2021, IOP Publishing Ltd.

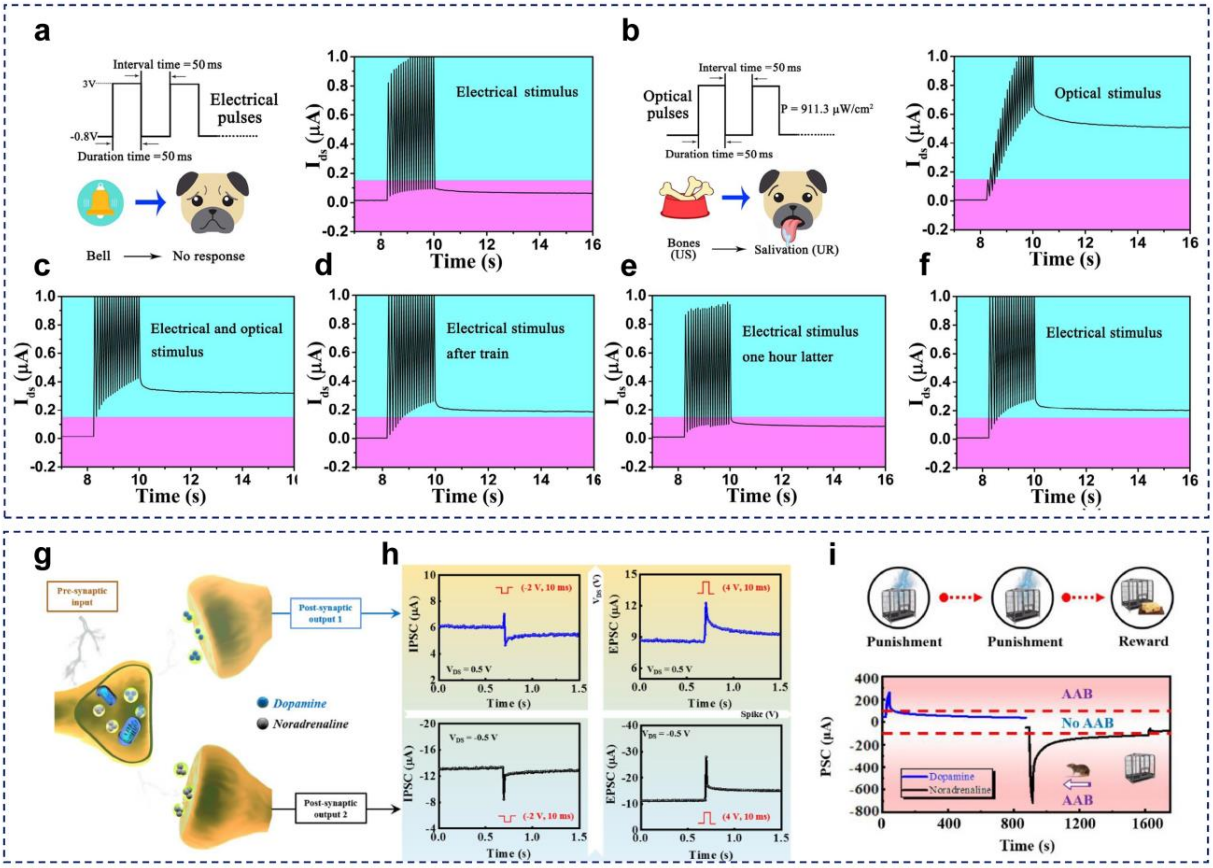

Figure 15. a) EPSC after electrical pulses stimulation (conditioned stimuli), no salivation response. b) EPSC after optical pulses stimulation (unconditioned stimuli), producing unconditioned salivation response. c) Training by electrical and optical pulses for 20 cycles to build associative reflex between unconditioned stimuli and conditioned stimuli. d) After training, only electrical pulses can produce salivation response. e) After 1 h, the associative reflex is forgotten, and electrical pulses cannot produce salivation response. f) Re-training for 10 cycles, and association with 20 electrical spikes can produce salivation response. Reproduced with permission.[126] Copyright 2019, Elsevier Ltd. g) Schematic illustration of dopamine and norepinephrine transmission in the synaptic cleft under different internal environments. h) PSCs of ZnO NW-based neuromorphic device under different external spikes and internal environment. i) Schematic demonstration and implementation of Skinner Box using ZnO NW-based neuromorphic device. Reproduced with permission.[75] Copyright 2021, Elsevier Ltd.

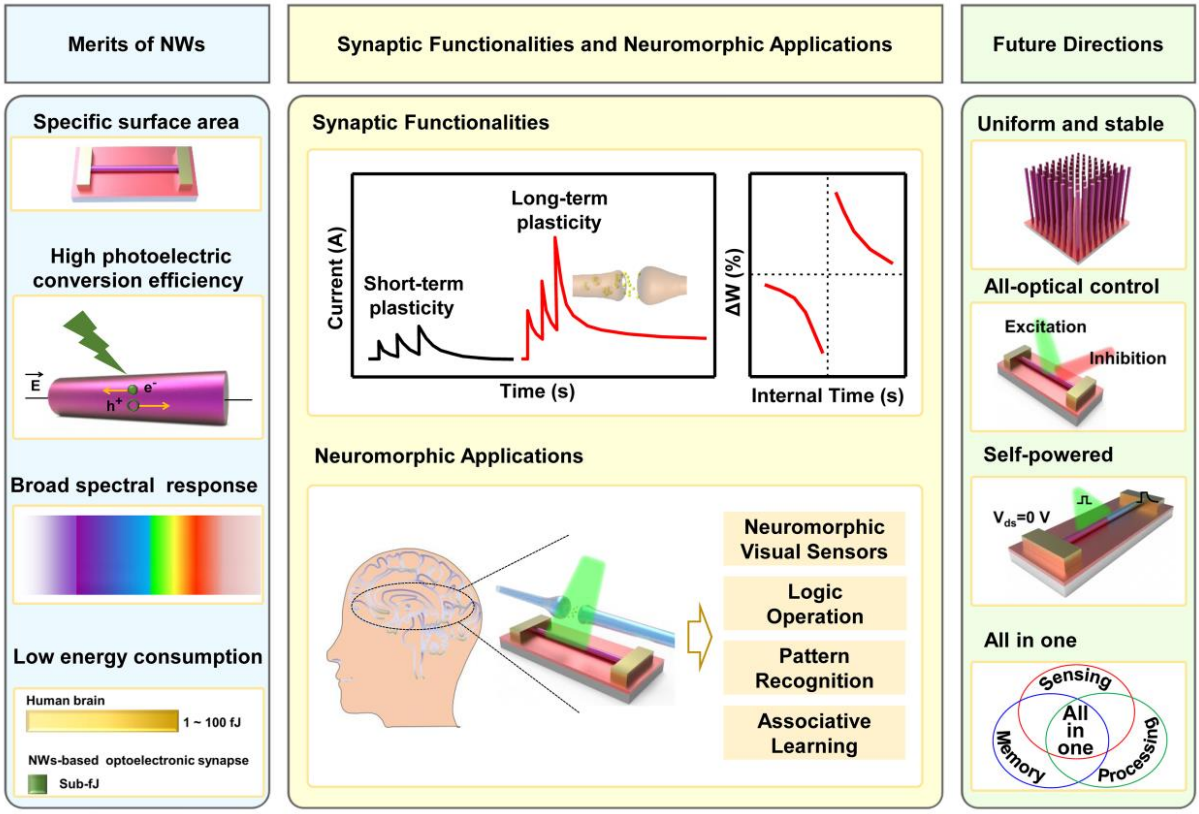

Figure 16. The advantages, current status and future directions of NWs based optoelectronic synaptic devices.

Table 1. The comparison of key characteristics for electronic, optoelectronic, and pure photonic synapses.

Synaptic devices	Speed of neural operations	Complexity of preparation process	Power consumption	
			Electrical power consumption	Optical power consumption
Electronic synapses	+	+	+ +	
Optoelectronic synapses	+ +	+ +	+	+
Pure photonic synapses	+ + +	+ + +		+ + +

Table 2. A comparison of power consumption of various materials based optoelectronic synaptic devices.

Category	Material	λ (nm)	E (event−1) /Operation energy	Synaptic functions and neuromorphic application	Ref.
1D materials	$InGaO_3(ZnO)_3$ NW	261	0.7 fJ	STP-LTP, LTP/LTD, PPF, SNDP, STDP, human visual system	[37]
	Si NW	435, 550, 650	1 nJ	EPSC, IPSC, PPF, STP-LTP, SNDP, SRDP, dynamic filtering	[102]
	SnO_2 NW	275	338.7 pJ	EPSC, PPF, STP-LTP, SRDP, STDP, Pavlovian conditioning	[126]
	ZnO NW	365	1 pJ	EPSC, IPSC, PPF/PPD, LTP/LTD, STDP, image recognition	[50]
	Ag NW	365	4 μJ	EPSC, PPF/PPD, SRDP, STDP, Pavlovian conditioning	[129]
	TiO_2 NW	405	0.5 mW	STP, LTP, STDP	[130]
	SnO_2 NW	365	2.5 - 20 mW/cm^2	EPSC, PPF, SNDP	[49]
	InAs NW	633	10^{-5} - 1 W/cm^2	STP, LTP, PPF	[131]
	InGaAs NW	450, 1550	8 mW	LTP/LTD, Pavlovian conditioning	[39]
	Ag NWs	415 - 940	7×10^{-4} mW/cm^2	logic gate, image processing and recognition	[103]
	InAs NW	532	2 - 200 W/cm^2	STP-LTP, PPF	[132]
	ZnO NW	365	0.63 - 4.20 mW/cm^2	PPF, STP, LTP	[38]
2D materials	MoS_2	405	404 mW/cm^2	STP/STD, LTP/LTD, STDP	[133]
	WS_2	405 - 633	0.19 - 28 μw	STP-LTP, LTP/LTD, SNDP, SRDP	[134]
	BP	280, 365	3 - 6.8 mW/cm^2	STP-LTP, LTP/LTD, image processing and recognition	[135]
	MoS_2/h-BN	520	28.3 $\mu W/\mu m^2$	STP/STD, LTP/LTD	[136]
	MoS_2	445	26.67 fJ	STP/STD, LTP/LTD, STDP, Pavlovian conditioning	[41]
	BP	280, 365	8 fJ	STP, LTP, SRDP, PPF/PPD, STDP, Pavlovian conditioning	[40]
	graphene/h-BN/MoS_2	470	2.52 fJ	STP-LTP, LTP/LTD, PPF, SRDP, SNDP, pattern-recognition	[137]
0D materials	$MAPbI_3$/Si nanocrystals	375, 532, 808	4.58 - 1351 $\mu W/cm^2$	PPF, SNDP, SRDP, dynamic filtering	[138]
	$CsPbBr_3$ QDs	375	1.4 nJ	STP-LTP, PPF/PPD, LTP/LTD SRDP	[139]
	$MAPbBr_3$	440	36.75 pJ	PPF, SNDP, LTP/LTD, image recognition	[140]
	$Cs_{1-x}FA_xPbBr_3$ QDs	450	3×10^{-17} J	PPF, LTP/LTD, SNDP	[141]
3D materials	AlN	180 - 200	30 $\mu J/cm^2$	PPF, STP-LTP, LTP/LTD, SRDP, image recognition	[90]
	IGZO	350 - 750	0.12 - 70 $\mu W/cm^2$	STP, LTP, PPF, Pavlovian conditioning	[142]
	Si	635, 450	60 - 439 mW/cm^2	STP–LTP, PPF, Pavlovian conditioning, pattern recognition	[143]
	In_2O_3/ZnO	365	0.2 nJ	STP-LTP, PPT, LTP/LTD,	[128]

Table 3. Some typical NWs materials that exhibit positive or negative photoconductivity responses.

Materials	Photoconductivity Effect		Ref.
	positive	negative	
Si NWs	√	√	[102, 154]
Ge NWs	√	√	[155]
GaAs NWs	√		[76]
InAs NWs	√	√	[59, 156]
InGaAs NWs	√	√	[39, 157]
InAsSb NWs	√	√	[158]
ZnO NWs	√	√	[75, 159]
CdS NWs	√	√	[160]
GeS NWs		√	[161]
AlN NWs	√	√	[162]
ZnSe NWs	√	√	[163-164]
Cd_3As_2 NWs	√	√	[149, 165]

Xue Chen is currently a postdoctoral researcher at Shenzhen University. She received her Ph.D. degree from Changchun University of Science and Technology in 2021. Her research interests focus on high-performance nano-optoelectronic devices, such as data storage, artificial synaptic devices, and photosensors.

Prof. Ye Zhou is a Fellow of the Royal Society of Chemistry (FRSC), Fellow of the Institution of Engineering and Technology (FIET) and group leader at the Institute for Advanced Study, Shenzhen University. His research interests include flexible and printed electronics, organic/inorganic semiconductors, surface and interface physics, nanostructured materials, and nano-scale devices for technological applications, such as logic circuits, data storage, photonics and sensors.

Nanowires based optoelectronic synaptic devices are suitable for low power consumption neuromorphic applications due to their unique properties. Herein, we summarize the typical ultraviolet-visible-infrared materials and introduce the current progress of nanowires based optoelectronic synaptic devices in ultraviolet-visible-infrared spectral range, including the synaptic functionalities and neuromorphic applications. This review may promote nanowires for future multifunctional neuromorphic optoelectronic systems.

Xue Chen, Bingkun Chen, Bei Jiang, Tengfei Gao, Gang Shang, Su-Ting Han, Chi-Ching Kuo, Vellaisamy A. L. Roy and Ye Zhou*

Nanowires for Ultraviolet-Visible-Infrared Optoelectronic Synaptic Devices